Environmental Earth Sciences (2026) 85:418
https://doi.org/10.1007/s12665-026-13171-1

ORIGINAL ARTICLE

Analysis of amplifying effect of antecedent drought on rainfall-induced shallow landslides

Dogukan Tayyar[1,2] · Hakan Tanyas[2] · Resul Comert[3] · Anil Yildiz[4] · Tolga Gorum[5] · Nihat Sinan Isik[6] · Mehmet Ekmekci[1]

Received: 19 June 2026 / Accepted: 2 October 2026 / Published online: 8 October 2026
© The Author(s) 2026

Abstract
Rainfall-induced shallow landslides are typically attributed to short-term meteorological triggers such as rainfall intensity and duration. However, the influence of antecedent hydrological conditions, particularly prolonged dry spells, has received limited attention despite their potential to alter soil behavior significantly. This study investigates the role of antecedent dry spells on landslide occurrence in the clay-rich terrains of the eastern Black Sea region of Türkiye. Four intense rainfall events from two study sites were examined. At both sites, the later event followed a prolonged dry period and produced a substantially larger mapped landslide inventory despite lower landslide-day rainfall than the earlier event, which occurred under wetter antecedent conditions. To investigate the mechanisms underlying this behavior and evaluate whether it was evident across the event inventories, we combined mechanistic numerical simulations with a data-driven statistical analysis. Numerical simulations indicate that a configuration representing crack-related hydraulic and mechanical changes enhances infiltration and reduces matric suction, resulting in strength reduction and lower slope stability. Additionally, a Generalized Additive Model incorporating landslide-day precipitation, the 30-day Standardized Precipitation Index (SPI-30), local relief, slope steepness, and aspect reveals that landslides are more likely to occur when intense rainfall coincides with drier antecedent conditions rather than under persistently wet conditions. The model showed consistent discriminatory performance under grouped tenfold cross-validation, with an overall ROC AUC of 0.836 based on combined validation-fold predictions. These findings suggest that in clay-rich environments, conventional rainfall thresholds used in predictive models may underestimate landslide occurrence probability when preceded by dry spells. Incorporating antecedent drought indicators into forecasting frameworks may improve the representation of landslide probability, although validation across additional events and locations is required.

Keywords Dry Spell · Landslide · Rainfall · Numerical Modeling · Data-Driven Statistical Analysis

✉ Dogukan Tayyar
dogukantayyar@hacettepe.edu.tr

✉ Hakan Tanyas
h.tanyas@utwente.nl

[1] Hydrogeological Engineering Program, Hacettepe University, Ankara 06800, Türkiye

[2] Faculty of Geo-Information Science and Earth Observation (ITC), University of Twente, Enschede, AE 7500, the Netherlands

[3] Institute of Earth and Space Science, Eskisehir Technical University, Eskisehir, Türkiye

[4] Methods for Model-based Development in Computational Engineering, RWTH Aachen University, Aachen, Germany

[5] Eurasia Institute of Earth Sciences, Istanbul Technical University, Istanbul, Türkiye

[6] Department of Civil Engineering, Faculty of Technology, Gazi University, Ankara, Türkiye

Introduction

Early warning systems are an essential part of the near-real-time communication of natural hazard threats to society (Piciullo et al. 2018). This is also valid for landslides, where such systems should ideally account for the susceptibility of a given landscape, which is mainly controlled by morphometric, geologic, climatic, and anthropogenic characteristics (Guzzetti et al. 2020; Stanley et al. 2021; Ahmed et al. 2023). In practice, however, most landslide early warning systems rely on two parameters: rainfall intensity and duration (Mondini et al. 2023). These are often expressed as the total accumulated rainfall over a specific time window prior to a landslide event (e.g., Crosta 1998; Baum and Godt 2010; Segoni et al. 2018). Intensity-duration relationships are then used to define rainfall thresholds that inform the public about the potential hazard levels (Segoni et al. 2015). However, beyond rainfall intensity and duration, the antecedent conditions play a role in the initiation of landslides (Bhadiyadra and Ong 2024; Greco et al. 2023; Jayakody et al. 2023).

Recently, there has been a growing recognition of the critical role of antecedent hydrological conditions, leading to the development of predictive landslide models and early warning algorithms that leverage full precipitation time series or the temporal clustering of rainfall events (Mondini et al. 2023; Nocentini et al. 2023; Banfi et al. 2023; Fang et al. 2023; Lim et al. 2024; Moreno et al. 2025). These studies suggest that such an approach can improve landslide prediction accuracy compared to models relying solely on scalar meteorological proxies, as it also captures the influence of dry periods preceding the event.

Fredlund et al. (1978) and Vanapalli et al. (1996) extended Terzaghi's (1950) effective stress framework to account for unsaturated soil conditions. Their studies incorporated the contribution of matric suction to shear strength, providing a more comprehensive description of the relationship between effective stress and pore water pressure. This extension allows for a better understanding of how infiltration and changing suction conditions influence slope stability. However, another crucial factor influencing the relationship between rainfall intensity and slope stability is the antecedent dry spell preceding the rainfall event (Tichavský et al. 2019).

Dry spells may play a significant role from a geotechnical and hydrogeological perspective by inducing crack formation in clay-rich soils, which increases the secondary permeability of the upper layer of the soil (Dos Santos et al. 2016). This process could lead to an increase in pore water pressure and a decrease in soil shear strength and reduce surface runoff especially during intense rainfall events, consequently increasing the probability of landslide (Damiano et al. 2017; Cheng et al. 2021; Zhang et al. 2021). Furthermore, wetting-drying cycles can induce material deterioration and can lead to increased failures (Stirling et al. 2021). Gao et al. (2024) observe that when desiccation cracks significantly increase, forming additional flow paths for water infiltration leads to a substantial rise in the soil's hydraulic conductivity, which may in turn contribute to slope instability. Similarly, Apriyono et al. (2025) report that in prolonged dry seasons, crack intensity could increase up to 15%, leading to an increase in the soil's saturated hydraulic conductivity by over 85%. Understanding these mechanisms under extreme climate scenarios is crucial for improving current methods aimed at mitigating landslides attributed to intense rainfall.

This study examines the role of antecedent dry spells in modulating landslide occurrence preceding major rainfall events. The analysis focuses on two sites located in the eastern Black Sea region of Türkiye, where landslide inventories were compiled in association with distinct rainfall episodes (Çömert et al. 2025). At both sites, the later event followed a prolonged dry period and was associated with a substantially larger mapped landslide inventory despite lower landslide-day rainfall than the earlier event, which occurred without a pronounced antecedent dry spell. Although absolute inventory counts may also be influenced by differences in mapped area, imagery characteristics, and minimum detectable landslide size, this repeated contrast motivated an investigation of whether antecedent drying could amplify slope response to subsequent intense rainfall. To investigate the underlying behavior, two complementary but independent approaches are used. The numerical analysis examines a plausible local-scale hydro-mechanical mechanism, whereas the statistical analysis evaluates whether a corresponding association between triggering rainfall and antecedent precipitation conditions is evident across the event inventories. It is emphasized, however, that this contribution is not expected to be uniform across all settings. It is likely most relevant for clay-rich hillslope materials exposed to intense rainfall following prolonged dry periods, rather than a general feature of rainfall-induced landsliding.

Building on the repeated contrast observed at both study sites, we hypothesize that antecedent drying amplifies the response of clay-rich residual soils to subsequent intense rainfall. We examine this hypothesis by combining numerical simulations of crack-related changes in near-surface permeability and cohesion with a statistical analysis of the four event inventories to assess whether landslide probability increases when intense rainfall follows drier antecedent conditions, after accounting for terrain controls. The two analyses are interpreted as complementary lines of evidence rather than as formal cross-validation of one another.

Study area

This study focuses on sites within the Black Sea region, an area where approximately 55.5% of all reported fatal landslides in Türkiye occurred between 1929 and 2019 (Görüm and Fidan 2021). According to reported events between 1995 and 2014, this also refers to a region with the highest number of landslide-related fatalities in Europe (Haque et al. 2016). And yet, no rainfall early warning system exists in the study area (Görüm and Fidan 2021). The location map of the study is shown in Fig. 1, and the climatological factors underlying the region's markedly high rainfall totals (Fig. 1a) are discussed later in this section.

Four rainfall-induced shallow landslide events that occurred in Hopa and Kaptanpaşa, located in the provinces of Artvin and Rize, respectively, in the eastern Black Sea region of Türkiye, were analyzed. The study areas are characterized by steep and rugged topography (Fig. 1b), where the maximum elevation reaches up to 1,513 m. Although the Kaptanpaşa and Hopa domains are separated by a geographical distance of approximately 70 km, they belong to the similar morpho-climatic and lithological corridor of the eastern Black Sea coastal zone. Topographically, both sites are characterized by steep, deeply incised valleys driven by the same orogenic framework of the Eastern Pontides. Furthermore, they are subjected to the same severe orographic precipitation regime, governed by the parallel alignment of the mountain range to the coastline, which exposes both areas to similar extreme summer rainfalls.

Rainfall data for the selected sites were obtained from the General Directorate of State Meteorological Works and temperature information was obtained from ERA5-Land satellite (Fig. 2). The September 23, 2012 Hopa event, associated with approximately 340 mm of rainfall in a single day, triggered 26 landslides. In contrast, the August 24, 2015 event in the same area resulted in 1,367 landslides (Fig. 1b),

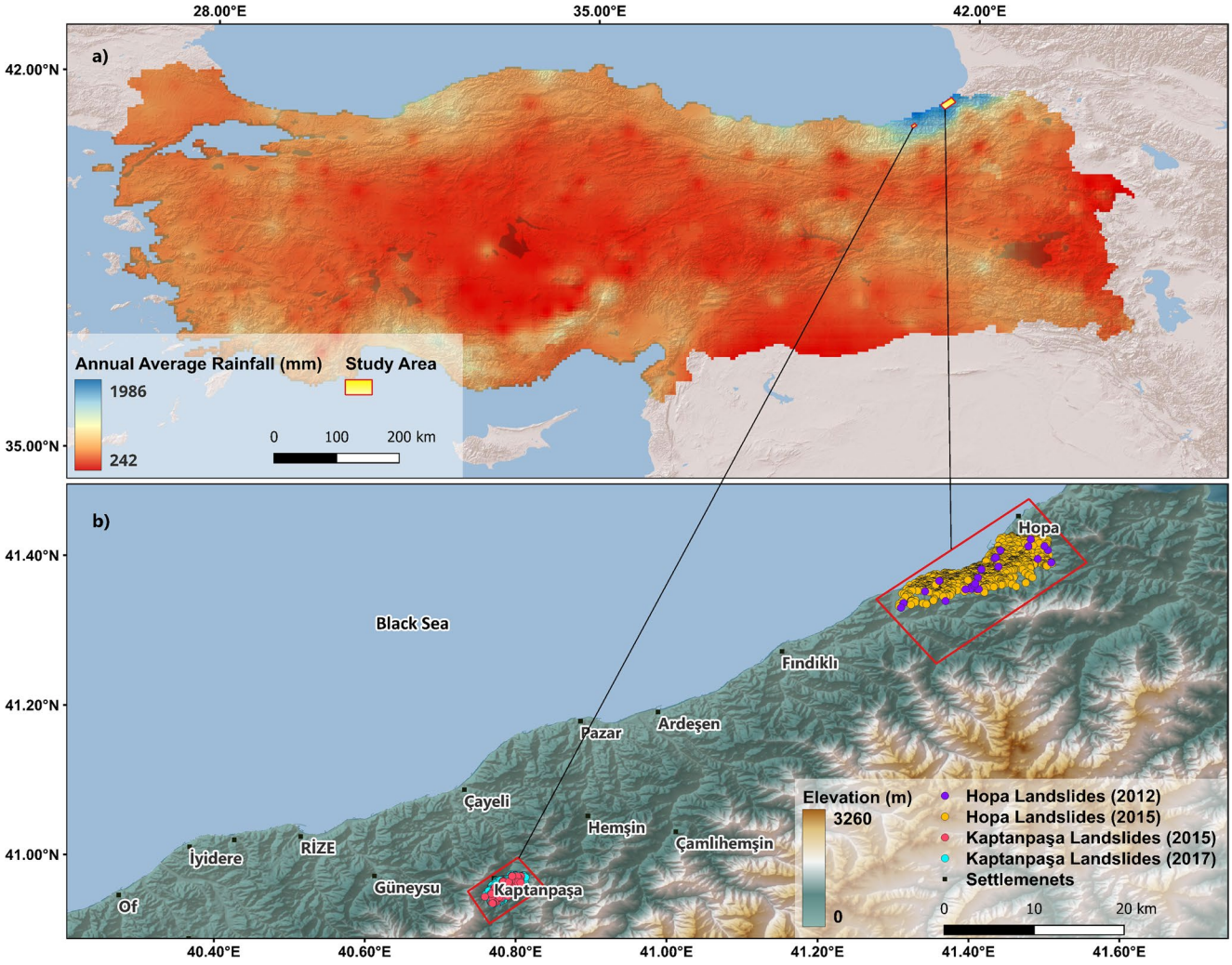

Fig. 1 Location map of study area (**a**) grids of long-term annual average rainfall estimated by the climate hazards group InfraRed precipitation with station data (CHIRPS) model (Funk et al. 2015) based on measurements between 1990 and 2025 of Türkiye and (**b**) location and landslide distribution map of the study area

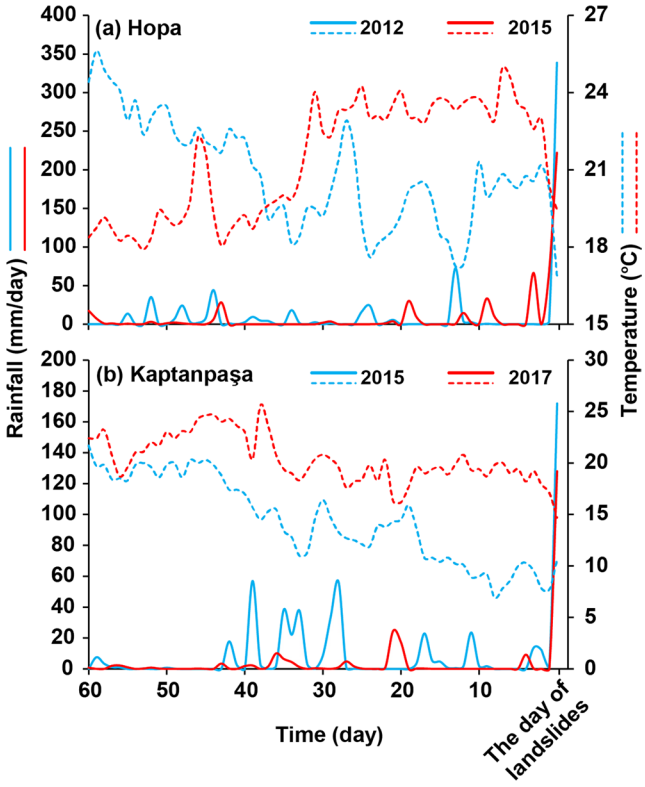

Fig. 2 60-day long rainfall and temperature time series generated for landslide events occurred in **a**) Hopa (September 23, 2012, and August 25, 2015) and **b**) Kaptanpaşa (November 12, 2015, and September 27, 2017)

Table 1 Summary of the four rainfall-induced shallow landslide events analyzed in this study (event inventories from Çömert et al. 2025)

Region	Event date	Daily rainfall (mm)	Antecedent condition	Landslides triggered	Role in this study
Hopa	23 Sep 2012	~340	No pronounced antecedent dry spell	26	GAM (statistical) only
Hopa	24 Aug 2015	~220	Preceded by a prolonged dry period	1,367	GAM (statistical) only
Kaptanpaşa	11 Nov 2015	~170	No pronounced antecedent dry spell ("wet" scenario)	67	Numerical model (unimodal)+GAM
Kaptanpaşa	27 Sep 2017	~130	Preceded by a prolonged dry period	1,142	Numerical model (bimodal)+GAM

despite a lower daily rainfall total of around 220 mm. Notably, the 2015 event was preceded by a prolonged dry period during the 60 days prior. A similar pattern was observed in Kaptanpaşa. The November 11, 2015 event, with approximately 170 mm of rainfall in a day caused 67 landslides, whereas the September 27, 2017 event, which was preceded by a dry period and triggered by around 130 mm/day of rainfall, led to 1,142 landslides (Fig. 1b). The key characteristics of the four analyzed events, including the daily rainfall totals, antecedent conditions, and number of landslides triggered, are summarized in Table 1.

The spatial distribution of the Kaptanpaşa and Hopa landslides was carefully mapped and verified using multi-temporal, high-resolution optical imagery across the entire study region by Çömert et al. (2025). As a representative example of this mapping process of Kaptanpaşa 2017 landslides, a small sub-area is presented in Fig. 3. The pre-event topographical and land cover conditions for this specific section were established using Google Earth imagery acquired on October 3, 2016, with a spatial resolution of 50 cm (Fig. 3a). Following the landslide events, extensive post-event morphological changes were captured via Unmanned Aerial Vehicle (UAV) flights on October 2, 2017. The resulting post-event images generated at an ultra-high spatial resolution of 12 cm, distinctly illustrate the widespread shallow landslides and exposed soil masses across the slopes (Fig. 3b). Using this detailed UAV imagery, the precise boundaries of the landslide source and runout areas were manually digitized to construct a highly accurate, event-based landslide inventory for the subsequent data-driven modeling (Fig. 3c).

In the Black Sea region, anthropogenic and meteorological disturbances are identified as the primary factors of landslide occurrences (Çömert et al. 2025; Reis et al. 2009; Nefeslioglu et al. 2011; Tanyaş et al. 2022). As for the meteorological conditions, extreme summer rainfalls occurring between July and September are reported as the main triggering factor for shallow landslides in the region (Yalcin 2007; Görüm and Fidan 2021). As illustrated by the long-term climatological data of the eastern Black Sea region (Fig. 4), this specific temporal window is critical, the region simultaneously experiences peak annual temperatures (averaging ~22 °C) and sustained high-intensity rainfall (maintaining monthly averages above ~160 mm).

Climatically, the region displays humid subtropical characteristics at low altitudes and temperate oceanic conditions at higher elevations, resulting in year-round precipitation and a relatively low likelihood of drought, mostly confined to the summer months (Yüksek et al. 2013). The long-term annual average rainfall in the study area reaches up to ~1990 mm especially in coastal parts (Fig. 1a).

Geological outline

The study area lies within the Eastern Black Sea Basin, a tectonic component of the Eastern Pontides characterized



Fig. 3 A representative small section of the high-resolution optical imagery utilized for landslide identification and inventory mapping in the broader Kaptanpaşa region. **a**) Pre-event Google Earth imagery (50 cm resolution) captured on October 3, 2016, showing intact slope conditions. (**b**) Post-event UAV-based orthomosaic (12 cm resolution) illustrating the widespread shallow landslides following the 2017 extreme meteorological event captured on October 2, 2017. (**c**) The corresponding UAV images with manually digitized landslide boundaries (red dashed lines) used to construct the spatial inventory

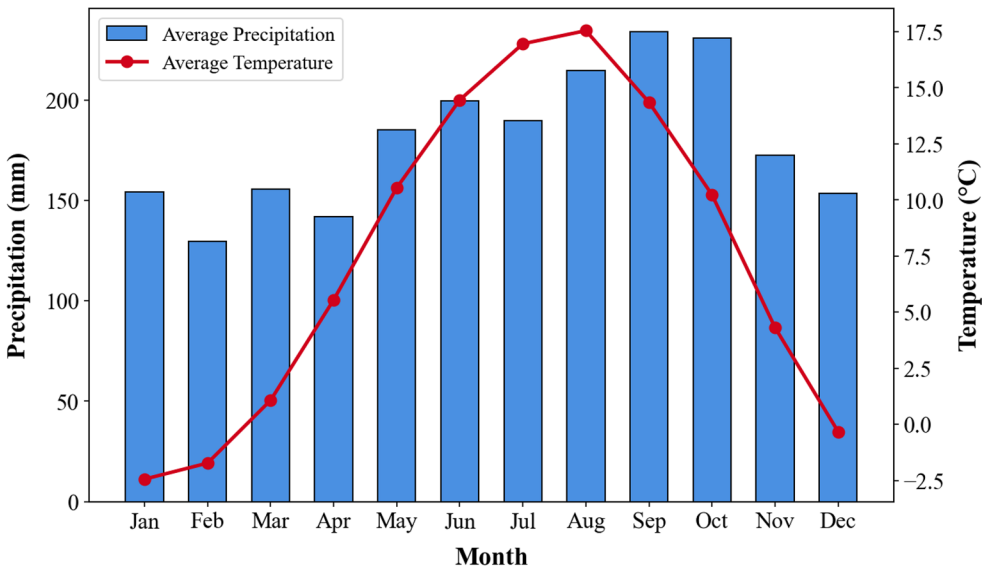

Fig. 4 Long-term (1990–2025) monthly average precipitation and temperature distribution for the eastern Black Sea region. The climatological data were derived from the ERA5-Land dataset, highlighting the critical June–September period characterized by peak annual temperatures and sustained high precipitation

by a Mesozoic–Cenozoic volcano-sedimentary and granitoid sequence overlying a Paleozoic crystalline basement (Alan et al. 2019; Tuysuz et al. 2008; Gedik et al. 1992). Locally, the stratigraphy comprises Upper Cretaceous to Middle Eocene volcano-sedimentary units (Çatak, Çağlayan, Çayırbağ, and Cankurtaran Formations), intruded by the Kaçkar Granitoids and capped by the Yeşilce Formation (Fig. 5). This predominantly volcanic and volcaniclastic lithology is the parent material for the fine-grained, clay/silt-rich residual soils described in Sect. 2.2, whose mineralogy, rather than the underlying bedrock stratigraphy itself, directly governs the desiccation and shrink–swell behavior central to the mechanism investigated in this study.

Uyeturk et al. (2020) investigated the geotechnical properties of residual soils associated with rainfall-triggered landslides in the same area, using X-ray diffraction (XRD) and Scanning Electron Microscopy (SEM) analyses to characterize the soil composition. Their results showed that the "total clay+mica" content in bulk samples ranges from 21.7% to 89.9%, with an average value of 66%. Specific analyses of the clay fraction demonstrated that halloysite is the most prevalent mineral, identified in 23 out of the 29 samples tested. In addition to halloysite, the clay fraction was found to commonly contain illite, kaolinite, vermiculite, and montmorillonite, alongside other minerals like gypsum and laumontite. Semi-quantitative analyses provided detailed insight into the clay composition, with one representative sample exhibiting 26.9% halloysite, 21.1% vermiculite, 11.2% montmorillonite, and 10.9% illite (Uyeturk 2019). Their study ultimately concludes that these residual soils are significant for their halloysite content, which can reach up to 27% within the clay fraction.

The desiccation behavior of halloysite is fundamentally dictated by its specific hydration state, as the mineral

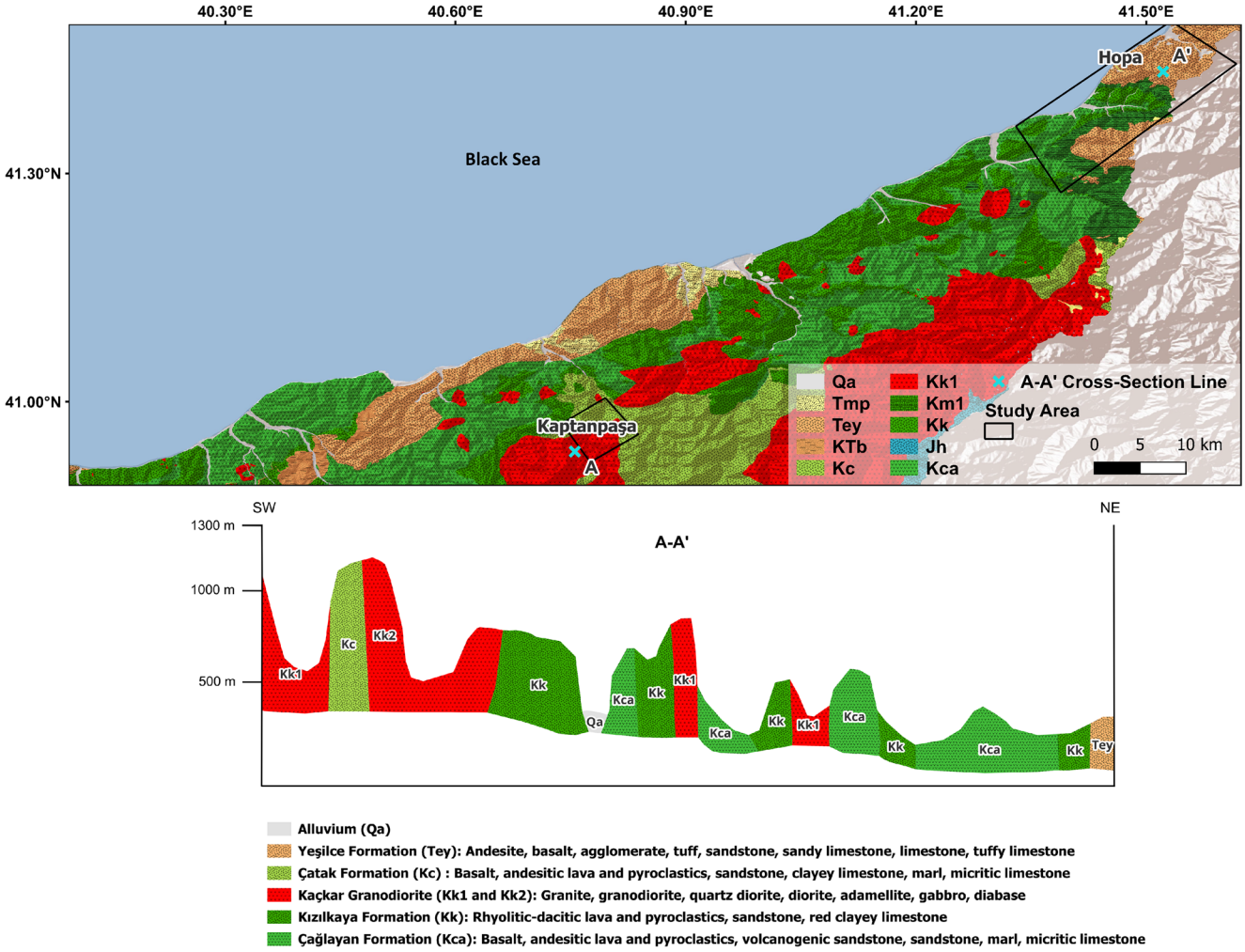

Fig. 5 Geology map and generalized cross-section (not-to-scale) of the study area

exists primarily in two distinct phases: the fully hydrated 10 A form (Halloysite- 10 A) and the dehydrated 7 A form (Halloysite-7 A) (Joussein et al. 2005). The phase transition from a hydrated to a dehydrated state represents a critical and irreversible process characterized by the expulsion of interlayer water molecules.

Engineering geology

The morphological characteristics of the 2017 Kaptanpaşa landslides were investigated in detail by Durmaz (2022) and Durmaz et al. (2023), who reported a mean failure depth of 1.05 m. The geotechnical parameters utilized in their study were adopted from Uyeturk et al. (2020) and subsequently used to perform model calibrations specific to the 2017 Kaptanpaşa landslides. Following the calibration of hydraulic and slope stability parameters, these studies established an effective cohesion (c') of 4 kPa, an internal friction angle (ϕ') of 30°, and a hydraulic conductivity (k) of 10^{-6} m/s.

The index properties of the soil samples provided by Uyeturk et al. (2020) were utilized to evaluate their swelling potential through a comparative analysis of the Holtz and Gibbs (1956), Dakshanamurthy and Raman (1973), and Skempton (1953) methodologies. The assessment framework prioritized Skempton's Activity index to identify mineralogical expansiveness, while relying on the convergence of high Liquid Limit (LL > 50%) and Plasticity Index (PI > 20%) values for samples lacking clay fraction data. The cumulative analysis reveals that approximately 51.5% of the specimens exhibit a Medium to High swelling potential, a behavior predominantly associated with the active clay minerals and organic constituents observed in the high-plasticity silt and organic clay (please see the Supplementary Materials, Table S1).

A literature review examined 30 geotechnical reports prepared by the Rize Provincial Disaster and Emergency Management Directorate (Altıgen Planlama & Zimer Mühendislik, 2024, please see the Supplementary Materials for

details). The results of the geophysical studies and laboratory experiments conducted within this scope are summarized in Table S2.

Porosity and saturation ratios were calculated using natural form weight and water content and included in the table (assuming a specific gravity (Gs) of 2.65). The characterization data reveals a heterogeneous soil profile predominantly composed of fine-grained, low to high plasticity clays (CL, MH) and silts (ML), with localized intercalations of granular silty sands (SM) and gravels (GM) according to the Unified Soil Classification System. Mechanical assessment through Standard Penetration Tests (SPT) indicated a wide range of in-situ stiffness, varying from loose deposits to refusal, which correlates with the observed increase in shear wave velocities (Vs) at greater depths. According to Vs measurements, a weathered residual soil with a velocity of 215–385 m/s was detected up to a depth of 5–10 m. Similar findings were also obtained with multi-electrode seismic tomography. Another study conducted by Keles and Nefeslioglu (2021), in which resistivity measurements along several profiles in the Rize province revealed that the soil thickness varied between 5 and 10 m.

Furthermore, phase relationship analyses derived from measured natural unit weights (γn), which ranged between 1.62 and 1.96 g/cm³ and yielded porosity values (n) between 0.31 and 0.49. Consequently, the calculated degrees of saturation (Sr) varied from approximately 32.5% to 84.3%, suggesting that the near-surface soil layers are primarily in a partially saturated state, a critical factor for subsequent effective stress and settlement analyses (Table S2).

Geotechnical reports in the region consistently characterize the geological setting of landslide zones as a complex assemblage of basalt, andesite, and pyroclastic units intercalated with sedimentary layers. Consistent with these findings, the study area exhibits a similar volcanic-sedimentary lithology. Reports also indicate that shallow slope slips are common within these geological units.

By synthesizing the comprehensive dataset compiled for the Rize region, a conceptual model has been developed to elucidate the failure mechanisms of shallow landslides triggered by high-intensity rainfall following prolonged drought periods in Kaptanpaşa. The proposed model and the governing parameters are detailed in the subsequent sections.

Materials and methods

A dual-method framework consisting of two independent but complementary approaches was adopted (Fig. 6): (1) a physically based numerical model used to investigate the local hydro-mechanical effects of antecedent drying on slope stability, and (2) a multi-event data-driven model used to evaluate whether a corresponding association between antecedent precipitation conditions and landslide occurrence was evident across the event inventories. The numerical and data-driven analyses were conducted as independent parallel frameworks because they operate at different spatial scales and rely on different data structures and assumptions. The numerical model simulated local transient hydro-mechanical responses, whereas the statistical model evaluated associations between landslide occurrence, triggering rainfall, antecedent precipitation conditions, and terrain characteristics. The two analyses were therefore interpreted as complementary lines of evidence for the hypothesized amplifying effect of antecedent drying rather than as a formal cross-validation of one another.

Numerical analyses were conducted using meteorological data from the Kaptanpaşa region and focused on the 60-day period preceding the 2015 and 2017 landslide events. This site was selected because the geotechnical parameters required for slope-stability modeling were available from previous studies in the area (Uyeturk et al. 2020; Durmaz et al. 2023). A transient seepage analysis was first conducted, after which the factor of safety was calculated throughout the 60-day period using the resulting pore-water-pressure distributions. The analysis was performed in two stages. First, a standard unimodal soil-water characteristic curve, representing an intact soil matrix, was applied to both the 2015 event, which occurred under wetter antecedent conditions, and the 2017 event, which followed a prolonged dry period. This provided a common hydro-mechanical baseline. The 2017 event was then reanalyzed using a bimodal soil-water characteristic curve and reduced near-surface cohesion to represent plausible crack-related hydraulic and mechanical changes associated with antecedent drying.

The data-driven analysis used four landslide-event inventories compiled for the Kaptanpaşa and Hopa regions (Çömert et al. 2025). The inventories were produced through systematic manual interpretation of high-resolution optical datasets, including RapidEye imagery at 5 m resolution, Google Earth imagery at approximately 0.5 m resolution, PlanetScope imagery at 3 m resolution (Planet Team 2017), and UAV-derived orthomosaics at 0.12 m resolution. Most mapped landslides were classified as shallow-seated slides occurring within the soil cover and were delineated as polygons (Çömert et al. 2025). Using these inventories, a binomial generalized additive model was developed at the slope-unit level to relate landslide occurrence to landslide-day precipitation, antecedent precipitation conditions represented by the 30-day Standardized Precipitation Index, local relief, slope steepness, and aspect. Model performance was evaluated using grouped tenfold cross-validation, with observations from the same physical slope unit retained within a single fold.

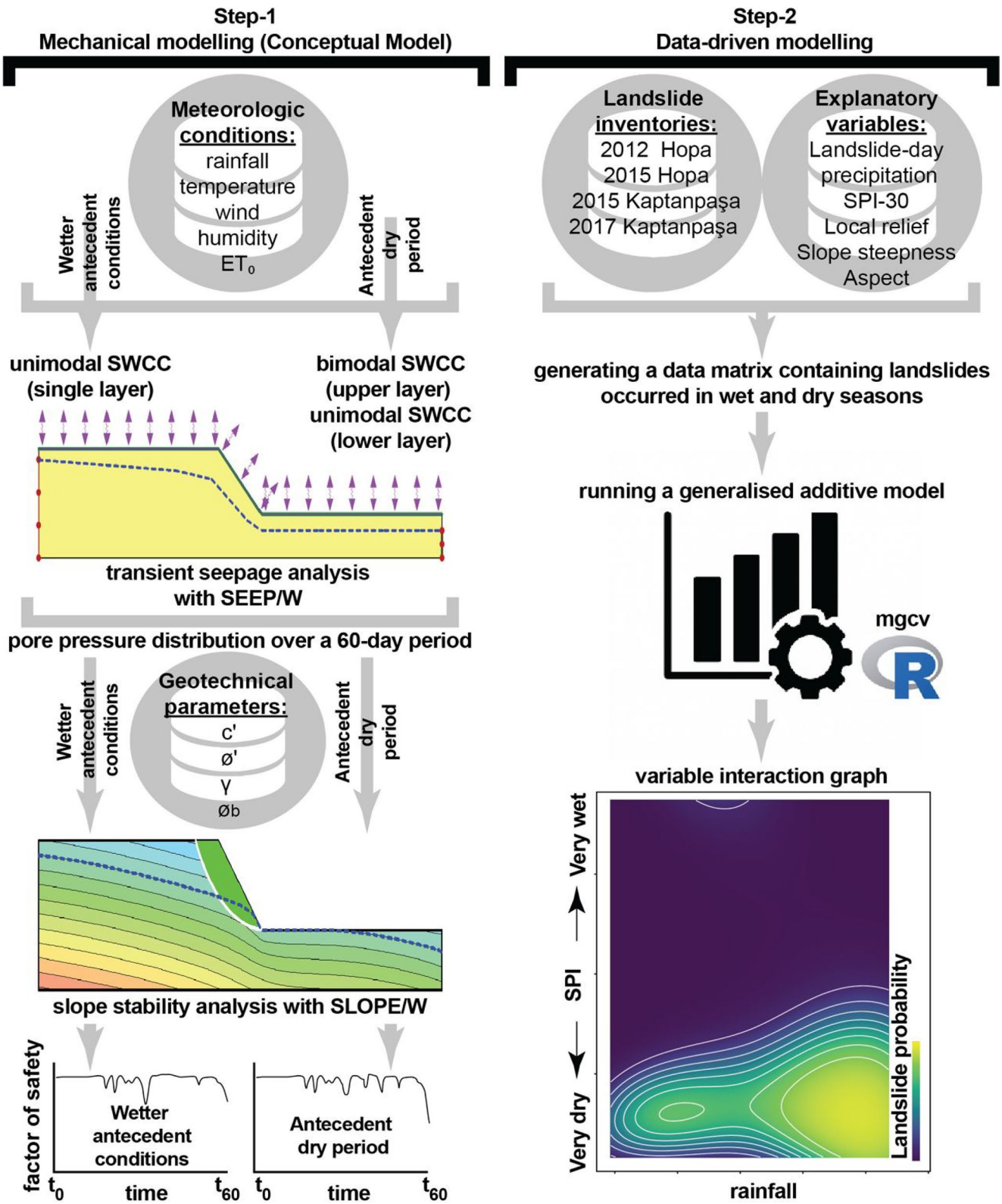

Fig. 6 Flowchart summarizing the two-step methodological framework, including mechanical and data-driven modeling, used to assess the role of dry spells in the occurrence of rainfall-triggered landslides

Numerical modeling

The conceptual model was constructed using the SEEP/W and SLOPE/W modules of GeoStudio (Seequent 2022), which have been widely used in the relevant literature (e.g., Erdağ and Işık 2022; Gasmo et al. 2000; Li et al. 2016; Qi and Vanapalli 2015; Rahardjo et al. 2007; Tsaparas et al. 2002).

Seepage model through SEEP/W

SEEP/W simulates water flow and pore-water pressure in both saturated and unsaturated soils using Darcy's Law:

$$q = k.i \tag{1}$$

Where q refers to the specific discharge, k denotes the saturated hydraulic conductivity and i represents the hydraulic gradient. The transient seepage is governed by:

$$\frac{\partial}{\partial x}\left(k_x \frac{\partial H}{\partial x}\right) + \frac{\partial}{\partial y}\left(k_y \frac{\partial H}{\partial y}\right) + Q = \frac{\partial \theta}{\partial t} \tag{2}$$

Where k_x and k_γ denote the hydraulic conductivity in the x and y directions, respectively, H represents the hydraulic head, Q is the source or sink term, θ stands for the volumetric water content and t refers to time.

In unsaturated conditions, volumetric water content changes depend on matric suction ($u_a - u_w$) since pore-air pressure (u_a) is assumed constant. This leads to:

$$\partial \theta = m_w \partial uw \tag{3}$$

Where m_w is the slope of the soil-water characteristic curve / compressibility coefficient of water.

The final governing seepage equation includes the unit weight of water, γ_w:

$$\frac{\partial}{\partial x}\left(k_x \frac{\partial H}{\partial x}\right) + \frac{\partial}{\partial y}\left(k_y \frac{\partial H}{\partial y}\right) + Q = m_w \cdot \gamma_w \cdot \frac{\partial H}{\partial t} \tag{4}$$

For slope stability analysis, the effective stress principle (Terzaghi 1950) and its extensions to unsaturated soils are applied. The shear strength τ is expressed as (Fredlund et al. 1978; Vanapalli et al. 1996):

$$\tau = c' + (\sigma - u_a)\tan\phi' + (u_a - u_w)\tan\phi^b \tag{5}$$

$$\tau = c' + (\sigma - u_a)\tan\phi' + (u_a - u_w)\left[\frac{\theta - \theta_R}{\theta_S - \theta_R}\right]\tan\phi' \tag{6}$$

Where c' is the effective cohesion; σ represents the total normal stress, u_a is the pore-air pressure, u_w is the pore-water pressure, ϕ' refers to the effective angle of internal friction and ϕ^b indicates the rate of increase in shear strength with matric suction. Additionally, θ is the volumetric water content, θ_R is the residual water content and θ_S is the saturated water content.

SEEP/W can simulate soil-vegetation-atmosphere transfer processes across the ground surface by employing the land–climate interaction (LCI) boundary condition. It provides a robust framework for evaluating water balance components and quantifying net percolation through system (Seequent 2022). At the LCI boundary condition, the water balance is calculated by conservation of mass:

$$(q_P + q_M)\cos(\alpha) + q_E + q_R = q_I \tag{7}$$

Where the superscripts used for water fluxes (q) represent different conditions; P is precipitation, M is snowmelt, I is infiltration, E is evapotranspiration, R is surface runoff and α is slope angle. Potential evapotranspiration (ET0) values were estimated using the Thornthwaite model (Thornthwaite 1948) and inserted into SEEP/W as user-defined values. Root water uptake and canopy interception have not been considered in this study.

Precipitation, temperature, wind speed, relative humidity, and potential evapotranspiration data for the 60-day periods preceding the landslide events in 2015 and 2017 in Kaptanpaşa were gathered from the Çayeli/Kaptanpaşa meteorological station, provided by the General Directorate of State Meteorological Works (Fig. S1).

The conceptual model used in this study is given in Fig. S2. The left and right boundaries were defined as hydraulic head boundaries (red lines with dots), the upper boundary as a LCI boundary, and the lower boundary as an impermeable boundary. The slope angle was taken as 45°. To minimize the influence of boundary conditions, the model boundaries were extended by 25 m. The soil thickness was determined based on studies as mentioned in engineering geology section, a soil thickness of 10 m was adopted in the model. Also, an initial water table (dashed blue lines), compatible with topography was used to define the initial conditions. The depth of the groundwater table was determined based on field investigations and water-level measurements obtained from nearby wells located north of the study area in the Çayeli district (15 km to northwest of study area). Observations revealed that the groundwater level remains close to the ground surface, and during the rainy season, water discharge occurs through fissures and cracks. In the conceptual model developed for this study, the average groundwater table is represented at a relatively shallow depth, typically between 2 and 4 m, to simulate more critical

conditions for slope instability. The initial pore-water pressure distribution for each transient simulation was defined as hydrostatic with respect to the assumed initial water table position (Fig. S2). Pore-water pressures below the water table increased linearly with depth, while pressures above the water table were assigned negative values consistent with the initial position on the adopted SWCC.

Due to absence of direct measurement, saturated hydraulic conductivity is estimated based on the studies of Uyeturk et al. (2020), Durmaz et al. (2023) and reports of Altıgen Planlama & Zimer Mühendislik (2024). The results of soil classification from different landslide sites at Rize show that in general the soil samples are fine-grained, low to high plasticity clays (CL, MH) and silts (ML), with localized intercalations of granular silty sands (SM) and gravels (GM) according to the Unified Soil Classification System. Based on this information, appropriate saturated hydraulic conductivity values were selected from appropriate range in the literature follows of 2 m/d (2.32×10^{-5} m/s) for the single-layer model, while for the bimodal SWCC case, values of 3 m/d (3.47×10^{-5} m/s) and 2 m/d (Freeze and Cherry 1979) were used for the upper and lower layers, respectively.

Due to the absence of direct measurements, saturated hydraulic conductivity is estimated based on the studies of Uyeturk et al. (2020), Durmaz et al. (2023) and reports of Altıgen Planlama & Zimer Mühendislik, (2024). The results of soil classification from different landslide sites at Rize show that in general the soil samples are fine-grained, low to high plasticity clays (CL, MH) and silts (ML), with localized intercalations of granular silty sands (SM) and gravels (GM) according to the Unified Soil Classification System. Based on this information, appropriate saturated hydraulic conductivity values were selected from appropriate range in the literature follows of 2 m/d (2.32×10^{-5} m/s) for the single-layer model, while for the bimodal SWCC case, values of 3 m/d (3.47×10^{-5} m/s) and 2 m/d (Freeze and Cherry,1979) were used for the upper and lower layers, respectively. This value was derived by cross-checking the soil classification reported by Uyeturk et al. (2020), the permeability behavior of fissured clay described by Qi and Vanapalli (2015) and falls within the plausible literature range for silty clay/silt soils (Freeze and Cherry, 1979). It is noted that this value is somewhat higher than the single back-calculated conductivity reported by Durmaz et al. (2023) for the same landslide ($\sim 10^{-6}$ m/s). This is consistent with the expectation that the near-surface, weathered and secondarily porous residual soil exhibits higher permeability than the more homogeneous, deeper conditions typically represented in a single back-analysis calibration.

To represent the SWCC under wet and dry seasonal conditions, different modeling approaches were adopted. For the wet season, the soil was modeled as a single homogeneous layer using a unimodal SWCC (e.g., Gasmo et al. 2000; Tsaparas et al. 2002; Rahardjo et al. 2007; Erdağ and Işık 2022). Under prolonged dry conditions, the conceptual model was divided into two layers: a cracked upper (surface) layer modeled with a bimodal SWCC, and an intact lower layer represented with a unimodal SWCC. To ensure methodological rigor and to verify whether this specific configuration is essential to explain the observed field phenomenon, the 2017 dry scenario was systematically tested using both the standard single-layer unimodal and the two-layer bimodal SWCCs. It is hypothesized that the physical characteristics of the cracks (e.g., density, aperture, and connectivity) govern the resulting increase in soil permeability, and that this effect can be represented by modeling the cracked layer as a high-permeability zone described by a bimodal SWCC.

Prolonged dry spells, particularly in clay-rich soils, can lead to the formation of desiccation cracks. These cracks increase the saturated hydraulic conductivity (Apriyono et al. 2025) while reducing the shear strength parameters of the affected zone (Pineda et al. 2014; Qi and Vanapalli 2015). Therefore, with these configurations, the effects of desiccation cracking were simulated with a bimodal SWCC (Fredlund et al. 2010; Li et al. 2011; Qi and Vanapalli 2015), as cracks function as macropores, allowing rapid drainage between the first air-entry value (1st AEV) and the onset of residual suction. After this point, drainage progresses through micropores, governed by the second air-entry value (2nd AEV).

Since there are no direct measurements of SWCCs for the study area, bimodal and unimodal SWCCs (Fig. S3) were generated according to the studies of Qi and Vanapalli (2015). In this context, all necessary information about bimodal SWCC can be found in the study of Qi and Vanapalli (2015).

The adoption of the Qi and Vanapalli (2015) SWCC is grounded in a comparable classification of shrink–swell behavior rather than an assumption of mineralogical identity. Qi and Vanapalli (2015) characterized a heavily overconsolidated, montmorillonite-dominated expansive clay (Regina clay, Saskatchewan, Canada), selected specifically because its pronounced desiccation cracking and dual-porosity behavior made it a well-documented reference case for bimodal SWCC modeling. The residual soils examined in the present study (Uyeturk et al. 2020) differ in dominant clay mineralogy, halloysite rather than montmorillonite but exhibit a comparable expansive classification. Approximately 51.5% of the tested specimens were rated as having Medium to High swelling potential based on Skempton's Activity index and Liquid Limit/Plasticity Index criteria (Sect. 2.2; Table S1), and montmorillonite was identified as a minor but present clay-fraction constituent (up to 11.2%)

alongside halloysite. Qi and Vanapalli (2015) SWCC was therefore adopted as a representative analogue for a soil of comparable shrink–swell classification and crack-forming behavior, rather than as a quantitatively calibrated match to the study area.

In the numerical model, the representation of incorporation crack development is based on experimental evidence from the literature. Tang et al. (2010) reported that initial cracks can appear in soil samples within just two days under 22 °C laboratory conditions. Furthermore, Luo et al. (2025) observed that crack depths progressively increase and stabilize over extended drying–wetting cycles. During the prolonged antecedent dry spell preceding the Kaptanpaşa 2017 event, the field conditions similar to these experimental environments, the soil was exposed to sustained mean temperatures of ~22 °C coupled with infrequent, extremely low-intensity rainfall (1–10 mm). Based on these conditions, significant cumulative structural degradation was assumed. The 2017 pre-failure conditions were directly characterized using a bimodal SWCC (a two-layer cracked medium) to accurately represent the severely desiccated state of the soil matrix at the onset of the triggering extreme rainfall.

In the literature, desiccation crack depths have been reported up to approximately 50 cm (Sander and Gerke 2007; Zhang et al. 2014; Pouya et al. 2019; Hassanikhah et al. 2022). However, it has also been mentioned that infiltration driven by preferential flow may extend to depths 4–5 times greater than the crack depth (Zhang et al. 2021). Accordingly, the upper layer representing cracks in the numerical model of the 2017 Kaptanpaşa landslide event (under dry conditions) was defined as 1 m.

Slope stability model through SLOPE/W

Slope stability was analyzed in SLOPE/W using limit equilibrium approach based on Spencer's method. The shear strength parameters were obtained from Uyeturk et al. (2020) (Table 2). The effective cohesion of the surface layer in dry conditions at the surface layer was assumed to be zero due to the degradation of shear strength parameters caused by desiccation cracks (Pineda et al. 2014; Qi and Vanapalli 2015). General assumption of the angle of shear strength contributes from matric suction (ϕ^b) is to be the two-thirds of the effective internal friction angle (ϕ') (Aversa et al. 2016; Erdağ and Işık 2022). The values tested ranging between 18° and 23° for ϕ^b.

Table 2 The shear strength parameters used in the numerical model (Qi and Vanapalli 2015; Uyeturk et al. 2020)

Material	Strength parameters			
	c' (kPa)	ϕ'	γ (kN/m^3)	ϕ^b
Cracked surface clay layer	0	27	18	18°-23°
Intact lower clay layer	4.4	27	18	18°-23°

Data-driven modeling

The data-driven analysis was performed using a binomial generalized additive model fitted with the mgcv package (version 1.9-4; Wood 2017) in the R programming environment (version 4.6.1; R Core Team 2026). Binomial GAMs are suitable for modeling a binary landslide-presence response and allow nonlinear relationships between landslide occurrence and the explanatory variables (Brenning 2008). The model was fitted to the combined dataset derived from the four landslide event inventories in Hopa and Kaptanpaşa (Çömert et al. 2025).

Slope units delineate individual hillslopes characterized by broadly similar geomorphological development and terrain orientation (Alvioli et al. 2016). Each slope unit was evaluated separately for each rainfall event. Therefore, each observation in the statistical dataset represents a specific slope unit under the meteorological conditions of a specific event. An observation was classified as a landslide presence when at least one mapped landslide intersected the corresponding slope unit during that event and as an absence when no landslide was mapped.

The combined dataset comprised 9,560 observations, including 1,203 landslide-presence observations and 8,357 landslide-absence observations. All available absence observations were retained, and no class balancing, oversampling, undersampling, or random absence selection was applied.

To evaluate the combined influence of triggering rainfall and antecedent precipitation conditions while accounting for spatial variability in terrain susceptibility, the model included a joint nonlinear term between landslide-day precipitation and the Standardized Precipitation Index calculated for the 30-day period preceding each event (SPI-30). The 30-day accumulation period was used to represent short-term antecedent precipitation conditions during the month immediately preceding each event. Landslide-day rainfall was excluded from the antecedent 30-day accumulation and modeled jointly with SPI-30 as a nonlinear interaction. Local relief, mean slope steepness, and aspect were additionally included as terrain-related explanatory variables. Aspect was represented using sine and cosine transformations to account for its circular nature.

Antecedent precipitation conditions were quantified using the Standardized Precipitation Index (SPI) developed by McKee et al. (1993) and further documented by Edwards and McKee (1997). SPI-30 was calculated from daily precipitation records. For each landslide event, precipitation was accumulated over the 30 days immediately preceding the event date. Rainfall recorded on the landslide day was excluded from this accumulation because it was included separately in the GAM as the short-term triggering-rainfall

predictor. Thus, SPI-30 was used to characterize antecedent precipitation conditions independently of the triggering rainfall.

For each event, the accumulated precipitation during the antecedent 30-day window was compared with precipitation totals calculated for the corresponding 30-day calendar period in each available year of the station record. The reference precipitation record extended from 1 January 1962 to 31 May 2020 for Hopa and from 11 December 2012 to 31 May 2020 for Kaptanpaşa. A gamma probability distribution was fitted to the historical 30-day precipitation totals, and the resulting cumulative probabilities were transformed into standard normal variates following the SPI framework of McKee et al. (1993). The calculations were performed using the SPI Generator software (National Drought Mitigation Center 2018). Negative SPI-30 values represent drier-than-normal antecedent conditions, whereas positive values represent wetter-than-normal conditions according to the classification presented in Table S3. The 30-day interval represents the antecedent timescale evaluated in this study and is not intended to constitute a universally optimal SPI timescale for rainfall-induced landslides.

Rainfall measurements were obtained from meteorological stations located within a 50-km buffer around each study area. For each event, landslide-day precipitation and SPI-30 were interpolated separately using inverse-distance weighting to generate spatially varying explanatory layers at a 30-m resolution. The corresponding values were summarized for each slope unit and combined with slope-unit measures of local relief, mean slope steepness, and mean aspect to construct the statistical analysis dataset.

The joint effect of landslide-day precipitation and SPI-30 was modeled using a tensor-product P-spline smooth specified with the t2() constructor in the mgcv package (Wood et al. 2013), allowing the relationship between triggering rainfall and landslide occurrence to vary nonlinearly with antecedent precipitation conditions. Zero-order difference penalties were applied to the P-spline coefficients, corresponding to ridge-type regularization, and smoothness was estimated using restricted maximum likelihood. Local relief and mean slope steepness were represented using ridge-penalized P-spline terms, whereas aspect was included through its sine and cosine components to preserve its circular nature. Landslide-day precipitation, SPI-30, local relief, and mean slope steepness were standardized before model fitting. During cross-validation, the means and standard deviations were estimated from each training subset and then applied to the corresponding validation subset. During cross-validation, the means and standard deviations used for standardization were estimated from the training subset and then applied to the corresponding validation subset. The fitted rainfall–SPI-30 interaction was visualized as a two-dimensional predicted-probability surface, with local relief and mean slope steepness held at their median values and aspect held at its circular mean. For this visualization, the final model was fitted to the complete dataset after completion of cross-validation.

Model validation was performed using stratified grouped tenfold cross-validation. The grouping variable combined the study area and slope-unit identifier, ensuring that repeated observations of the same physical slope unit from different events were assigned to the same fold. Slope-unit groups were stratified by study area and by the number of event inventories in which the slope unit contained a mapped landslide. Consequently, the same physical slope unit could not occur in both the training and validation subsets of a given iteration. In each fold, approximately 90% of the observations were used for model fitting and the remaining 10% for validation. This procedure was repeated across all ten folds so that each observation received one validation prediction from a model in which it had not been used for fitting. All validation metrics were calculated from the combined predictions from the ten validation folds. Because observations from all four events were represented across the ten folds, this procedure evaluated slope-unit discrimination within the observed event set rather than transferability to an entirely unseen rainfall event.

Model performance was evaluated using receiver operating characteristic analysis and the area under the receiver operating characteristic curve (ROC AUC). An ROC AUC of 0.5 indicates discrimination equivalent to random classification, whereas a value of 1 indicates perfect discrimination (Fawcett 2006). Because the dataset contained substantially more absence than presence observations, performance was also evaluated using the area under the precision–recall curve, which is informative for imbalanced binary datasets (Saito and Rehmsmeier 2015), and the Brier score, which measures the accuracy of probabilistic predictions (Brier 1950). The overall ROC AUC was calculated from the combined validation-fold predictions. Its 95% confidence interval was estimated using 2,000 grouped bootstrap resamples, in which physical slope units were sampled with replacement separately within each study area. Fold-specific ROC AUC values were also retained to assess variation in model performance across the ten validation folds.

Results and discussion

Numerical analysis results

The numerical analysis was conducted over a continuous 60-day period preceding the landslide events that occurred in Kaptanpaşa in 2015 and 2017. This extended timeframe

allowed us to accurately capture the transient hydrological conditions and the cumulative effects of the meteorological variables leading up to the failure. During the 60-day window preceding the 2015 event, temperatures progressively dropped below 20 °C, reaching approximately 8 °C by the landslide date on November 12 (Fig. 2b). This period was also characterized by several days of continuous rainfall exceeding 10 mm/day, with peaks reaching ~ 50 mm/day. In contrast, the 60-day period prior to the 2017 event experienced sustained temperatures around 20 °C, with only a single day of rainfall above 10 mm/day occurring approximately 20 days before the landslide (Fig. 2b). Consequently, the 2015 event was classified as occurring under relatively wet antecedent conditions, which maintained an intact soil matrix. Conversely, the 2017 event was preceded by a prolonged dry spell, providing the exact environmental conditions necessary for severe structural degradation and the presence of desiccation cracks prior to the triggering extreme rainfall.

To examine the influence of dry spells on landslide behavior, slope stability analyses were conducted using a single-layer unimodal SWCC and a two-layer bimodal SWCC under wet (2015) and dry (2017) conditions, respectively. In both cases, ϕ^b was taken as 23 degrees (Table 2).

The temporal variation of the FS over the continuous 60-day period revealed distinct hydro-mechanical responses among the 2015 wet conditions and the 2017 dry conditions (Fig. 7). Throughout the simulation, the two-layer model representing the 2017 dry conditions with a bimodal SWCC maintained a consistently lower FS than both the 2015 and 2017 single-layer unimodal counterparts. This lower FS reflects the faster infiltration enabled by the enhanced

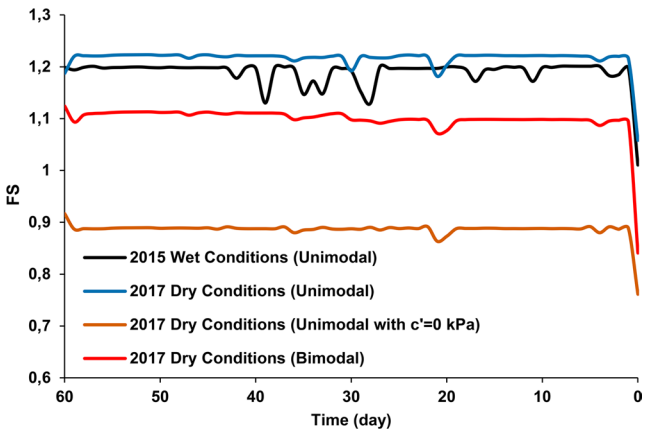

Fig. 7 Variation in the factor of safety over the 60-day period preceding the landslide events. The 2015 event represents wet antecedent conditions (unimodal SWCC, intact cohesion). The 2017 event is shown for three configurations used to isolate the role of cohesion loss in the desiccation-cracking hypothesis: unimodal SWCC with intact cohesion (c' = 4.4 kPa), unimodal SWCC with zero cohesion (c' = 0 kPa), and bimodal SWCC with zero cohesion (the configuration adopted as the working representation of the 2017 dry scenario in this study)

permeability of the cracked upper layer. At the end of the simulation period, coinciding with the triggering major rainfall event, the FS dropped abruptly across all models. However, the reduction was most critical in the 2017 bimodal model (dropping from approximately 1.10 to 0.84), indicating severe and sudden instability. In contrast, the 2015 wet conditions unimodal model, representing an initially intact and near-saturated soil matrix, experienced a more moderate decline (dropping from approximately 1.20 to 1.01). Similarly, when the 2017 dry conditions were simulated using a standard unimodal SWCC with intact cohesion (c' = 4.4 kPa), FS decreased only to about 1.06 and remained above the failure threshold throughout the 60-day period, indicating that meteorological forcing alone, without any assumed structural degradation, is insufficient to reproduce the observed failure.

To isolate the contribution of the mechanical (cohesion) component of the desiccation-cracking hypothesis, a decomposed configuration was additionally evaluated: a unimodal SWCC combined with zero surface cohesion. This configuration produced FS values below unity throughout the entire 60-day antecedent period, a pattern inconsistent with the absence of any observed landsliding during that window.

Only the fully combined configuration bimodal SWCC together with zero surface cohesion in the cracked layer reproduced a pattern consistent with field observations. FS remained above unity throughout the antecedent dry period, with a sharp reduction coinciding specifically with the triggering rainfall event. This comparison indicates that cohesion loss alone is necessary but not sufficient to reproduce the correct timing of failure without the accompanying change in SWCC, the model predicts persistent instability inconsistent with the observed absence of landsliding during the dry period. The enhanced macropore drainage represented by the bimodal SWCC appears to buffer the slope against premature failure during the antecedent period while still permitting rapid destabilization once intense rainfall occurs, consistent with the proposed dual-porosity infiltration mechanism.

Figure 8 shows the resulting pore water pressure distribution and critical slip surfaces, along with the corresponding FS on the day of the landslide occurrences. The results indicate that the 2015 Kaptanpaşa event, which occurred during a wet period, approached the critical stability threshold by day 60 (FS60 = 1.01). In contrast, the 2017 Kaptanpaşa event, which occurred under drier conditions, remained well below the critical level (FS < 1) by the end of the 60-day period (FS60 = 0.84). It is also notable that the critical slip surfaces identified for the two scenarios differ substantially in geometry (Fig. 8). The 2015 (wet) critical surface is deeper and spans a larger portion of the slope, whereas the 2017 (dry, bimodal) critical surface is confined to a shallow

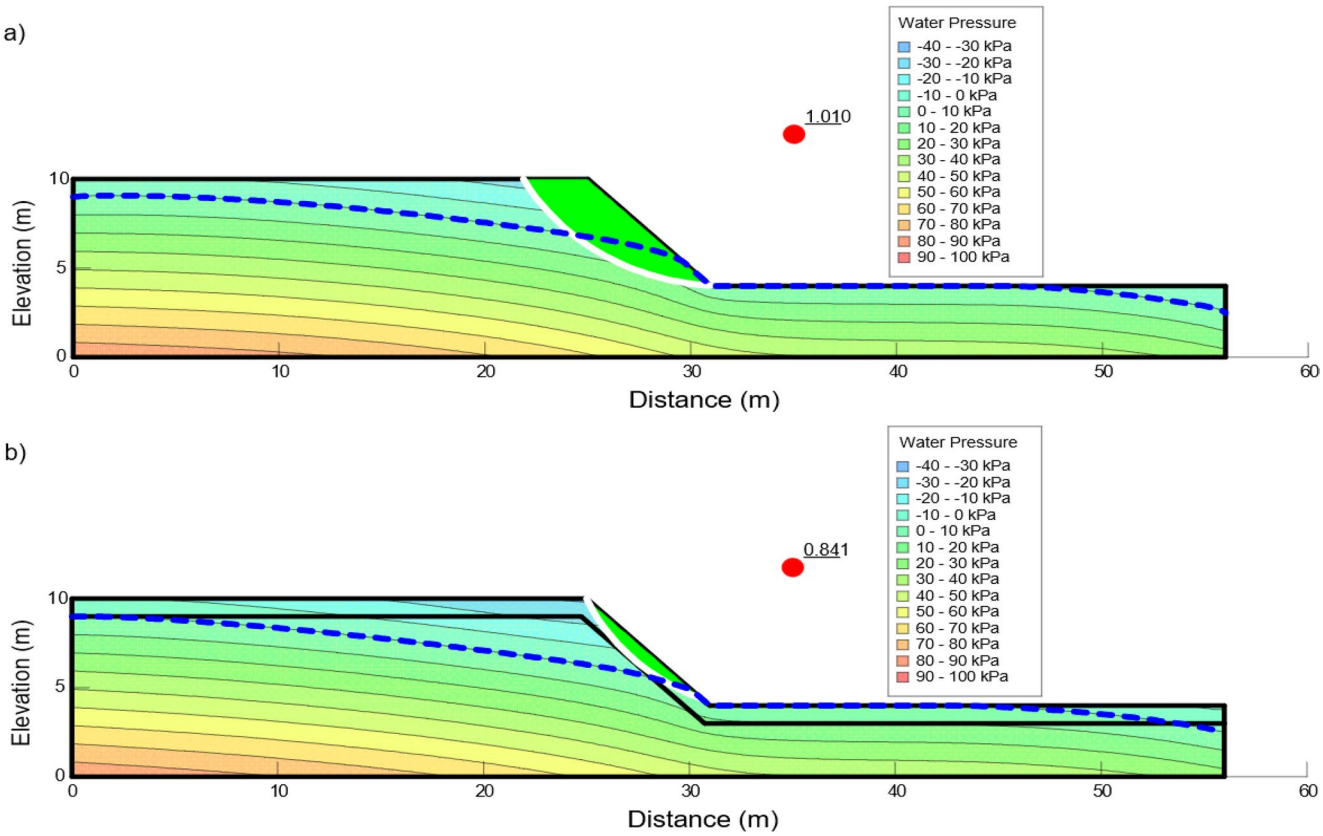

Fig. 8 Numerical analysis results for the Kaptanpaşa landslide events designed based on the conditions observed in (**a**) 2015 (wet conditions) and (**b**) 2017 (dry conditions/bimodal SWCC)

zone near the surface, consistent with the 1-m-thick cracked layer represented in the model. Because FS reflects the stability of a specific slip surface rather than the size of the resulting failure, a lower FS does not necessarily imply a larger or more hazardous landslide. This is, however, consistent with the empirical inventories. The 2017 dry event produced a far greater number of landslides (1,142) than the 2015 wet event (67), but these were predominantly shallow, small-volume failures, consistent with the shallow critical surface identified in the bimodal model. This is interpreted as a shift in failure mode from fewer, deeper failures under wet antecedent conditions to more numerous, shallow failures under dry antecedent conditions rather than a simple increase in the severity of a single failure mode.

The pore water pressure–time profiles are shown in Fig. 9 for four depths; the slope surface (0 m, purple), −0.5 m (red), −1.0 m (green), and −1.5 m (blue) with line style distinguishing the 2015 wet event (solid) from the 2017 dry event (dashed). Throughout most of the 30-day window, the 2017 (dashed) profile lies below its 2015 (solid) counterpart at every depth, reflecting the more negative pore water pressure (greater matric suction) sustained under antecedent dry conditions. At shallower depths, surface (purple) and −0.5 m (red), the 2015 profiles show two transient peak-and-decline

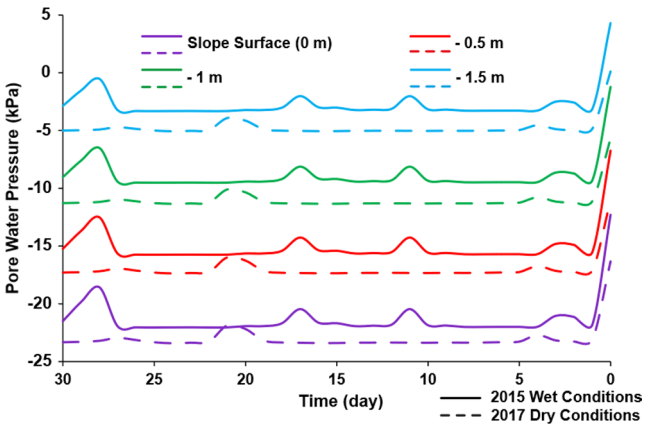

Fig. 9 The pore water pressure–time profiles at the middle of the slope surface and depths of −0.5 m, −1.0 m, and −1.5 m in 2015 wet conditions and 2017 dry conditions

cycles, consistent with intermittent rainfall pulses during the otherwise wetter 2015 antecedent period. These cycles are largely damped in the corresponding 2017 (dashed) curves, whereas the deeper profiles (−1.0 m, −1.5 m) remain comparatively smooth in both events. The most prominent feature of Fig. 9, however, is the sharp pore water pressure rise recorded at all four depths in the final days before failure

(day 0). Although this rise is qualitatively similar in both events, the 2017 (dry) curves ascend from a substantially lower pre-event baseline, so that the soil enters the triggering rainfall from a more negative suction state despite comparable final-day increments consistent with the lower FS60 obtained for 2017 relative to 2015 (Fig. 8).

Although the transient seepage simulations were conducted over a continuous 60-day period, the pore water pressure–time profiles presented in Fig. 9 deliberately focus on the final 30 days leading up to the landslide events. This narrowed temporal window was chosen to provide a higher-resolution visualization of the transient pore water pressure fluctuations, capturing the intricate hydro-mechanical responses at various depths immediately prior to failure.

Data-driven model results

The binomial generalized additive model showed consistent discriminatory performance under stratified grouped tenfold cross-validation. Based on the combined predictions from the ten validation folds, the overall ROC AUC was 0.836, with a 95% confidence interval of 0.826–0.845. The fold-specific ROC AUC values had a mean of 0.836 ± 0.018 and ranged from 0.810 to 0.873, indicating limited variation in discriminatory performance among the validation folds. The precision–recall AUC was 0.384. Because landslide presences accounted for 12.6% of the observations, the no-skill reference level for precision–recall performance was approximately 0.126. The observed value was therefore substantially higher than the class-prevalence baseline, indicating that the model distinguished landslide presences more effectively than a non-informative classifier despite the class imbalance (Saito and Rehmsmeier 2015). The Brier score was 0.091, representing the mean squared difference between the predicted probabilities and the observed binary outcomes (Brier 1950). The fold-specific receiver operating characteristic curves and the curve calculated from the combined validation-fold predictions are presented in Fig. 10a.

The fitted rainfall–SPI-30 interaction surface showed that predicted landslide probability depended jointly on landslide-day precipitation and antecedent precipitation conditions (Fig. 10b). Under negative SPI-30 values, representing drier-than-normal antecedent conditions, predicted probability generally increased with landslide-day precipitation. In contrast, predicted probabilities remained comparatively low under near-normal to positive SPI-30 values across most of the rainfall range shown. The modeled effect of triggering rainfall was therefore not uniform but varied according to the antecedent precipitation conditions.

These results are consistent with the hypothesis that antecedent drying can amplify slope susceptibility to subsequent intense rainfall within the four analyzed event inventories. However, the fitted surface represents a statistical association and should not be interpreted as establishing a universal rainfall or SPI-30 threshold or as independently demonstrating a specific causal mechanism. Furthermore, because observations from all four events were represented across the validation folds, the reported performance describes slope-unit discrimination within the observed event set rather than transferability to an entirely unseen rainfall event.

Discussion

Many regional scale landslide assessment examples in the literature showing a strong correlation between soil moisture and landslide occurrences (e.g., Zhao et al. 2019; Zhuo

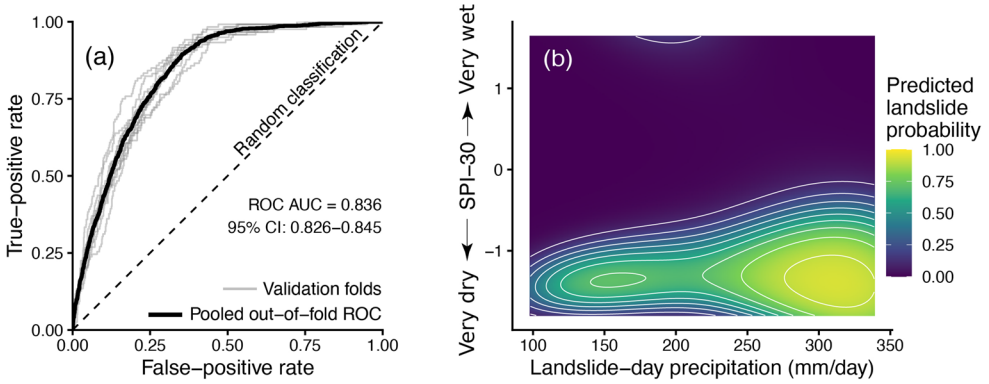

Fig. 10 Cross-validated performance and fitted rainfall–SPI-30 interaction of the binomial generalized additive model. (**a**) Receiver operating characteristic curves for the ten grouped validation folds, with observations from the same physical slope unit retained within a single fold. Gray curves represent the individual validation folds, the solid black curve represents the pooled out-of-fold predictions, and the dashed diagonal represents random classification. The pooled ROC AUC was 0.836 with a 95% confidence interval of 0.826–0.845, while the mean fold-specific ROC AUC was 0.836 ± 0.018. (**b**) Predicted probability of landslide occurrence as a function of landslide-day precipitation and SPI-30. Local relief and mean slope steepness were held at their median values, and aspect was held at its circular mean. The fitted surface represents the broad joint association between triggering rainfall and antecedent precipitation conditions and should not be interpreted as defining universal rainfall or SPI-30 thresholds

et al. 2019; Marino et al. 2020; Wicki et al. 2020). In this context, it is important to emphasize that results do not contradict existing literature but rather underscore a more specific condition in which extreme precipitation events may lead to more extensive landsliding when they are preceded by a dry period. Such dry periods could alter the shrinking-swelling response of clay-rich materials and if they are followed by an intense precipitation event, they could cause instabilities (Schulz et al. 2018). This means dry spells may not play a major role in landslides in all cases, but it is likely for clay-rich hillslope materials exposed to extreme summer rainfalls. In such cases, the rainfall thresholds estimated from intensity-duration relationships may also change. For instance, prolonged dry days may reduce the soil moisture content (Biniak-Pieróg et al. 2020) and increase the suction (negative pore water pressure) (Luo et al. 2023). Thus, the incoming rainfall could find surface conditions where the infiltration is promoted, favoring the sudden lubrication of a potential sliding surface at depth.

The traditional paradigm in landslide hazard assessment typically assumes that high antecedent soil moisture driven by prolonged pre-event rainfall is the primary prerequisite for slope failure, as it gradually raises the groundwater table and pore water pressures. However, this conventional hydrological explanation fails to account for the rapid failure mechanics observed during the 2017 Kaptanpaşa event, which occurred following an extended dry spell. An alternative explanation could be the presence of highly permeable relict joints, root decay channels, or animal burrows; however, these localized factors alone cannot explain the spatially distributed nature of the failures. Instead, the critical evaluation of the dual-method framework suggests that mechanical structural degradation (desiccation cracking) provides a more consistent explanation for the abrupt, dry-triggered failures observed in this study than the traditional hydrological pre-wetting mechanism alone. Desiccation cracking is not, however, proposed as the sole or dominant cause of the observed regional differences in landslide occurrence; rainfall intensity, slope and drainage conditions, land use, and other site-specific factors documented in the broader literature (e.g., Zhao et al. 2019; Zhuo et al. 2019; Marino et al. 2020; Wicki et al. 2020) are also expected to contribute, and the present results should be interpreted as evidence for an additional, previously underexplored contributing mechanism rather than a replacement for these established factors. The cracks effectively bypass the low-permeability soil matrix, fundamentally altering the infiltration boundary conditions from matrix flow to preferential dual-porosity flow. It is crucial to clarify the specific environmental and geotechnical boundaries within which this drought-cracking-infiltration mechanism is dominant. This phenomenon is strictly governed by the presence of fine-grained residual soils with significant clay/silt content and high swelling/shrinking potential. Furthermore, the proposed mechanism is dominant primarily within the shallow vadose zone (typically the upper 1.0 to 1.5 m), where thermal forcing and evaporation are most intense. Consequently, the applicability of this conceptual framework is strongly tied to regions experiencing seasonal climatic extremes, characterized by prolonged summer droughts immediately followed by convective, high-intensity rainfalls. It is emphasized that the desiccation-cracking mechanism investigated here is intrinsically linked to the shrink–swell behavior of clay/silt-rich soils and is not, by itself, expected to operate in coarse-grained or non-plastic materials lacking this mineralogical characteristic. This does not preclude the existence of analogous antecedent-drought effects in other soil types, for example, through drought-induced soil-water repellency, structural collapse, or root-decay-related macropore formation but such mechanisms would involve different physical processes and thresholds that fall outside the scope of the desiccation-cracking hypothesis tested in this study.

Under wet conditions (2015 event), rainfall infiltration led to rapid but limited increases in pore water pressure, with FS decreasing only marginally to the threshold of instability ($FS \approx 1.0$). This reflects a system that was already near saturation, where additional infiltration was constrained by reduced permeability and lower matric suction variability. Conversely, under the drier preconditions of 2017, even a moderate rainfall event induced a significant reduction in FS (from ~1.1 to ~0.84), indicating a more abrupt destabilization mechanism. The lower initial moisture contents in the upper soil layer, along with the development of desiccation-induced macropores, likely enhanced preferential flow pathways, accelerating infiltration toward the potential slip surface. Also, for dry conditions, an analysis was conducted using only the SLOPE/W package, excluding precipitation events. The analysis results (Fig. 11) showed the model to be stable ($FS = 1.028$). This indicates the extent to which precipitation, especially following a dry period, affects the system.

The comparison between unimodal and bimodal SWCCs further supports this interpretation. The bimodal model, representing a two-layer system with macro and micropore domains, consistently yielded lower FS values, particularly during rapid infiltration phases. This is consistent with the intended dual-porosity behavior of the bimodal SWCC formulation, whereby enhanced upper-layer hydraulic conductivity promotes faster saturation of deeper layers under cracked conditions.

These findings align with emerging global observations emphasizing the legacy effects of climate extremes on geotechnical infrastructure. The numerical and statistical outputs mutually confirm that severe summer desiccation

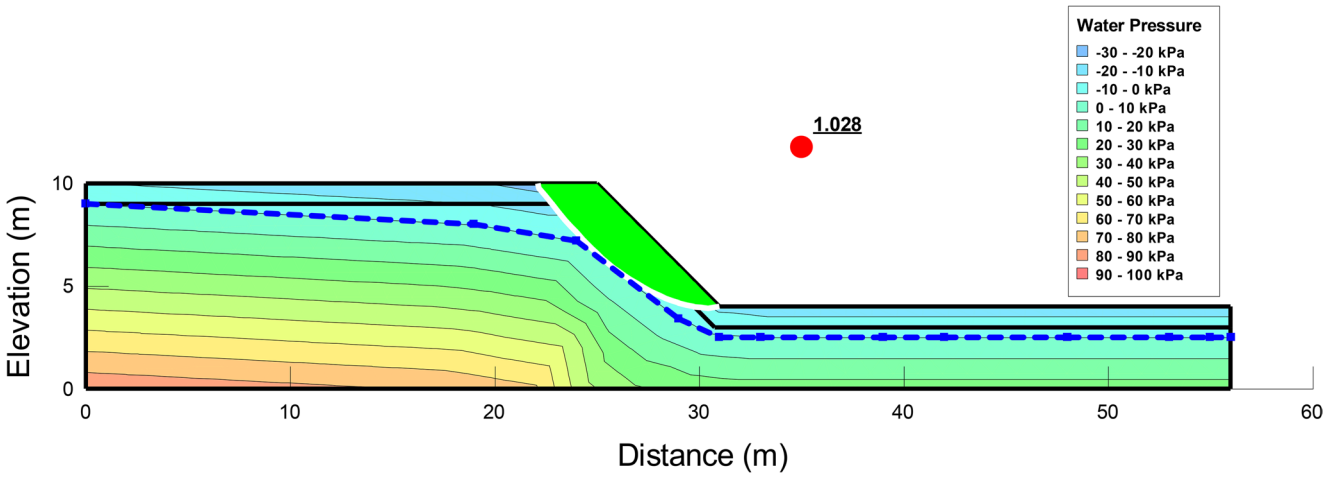

Fig. 11 Numerical analysis results for the 2017 Kaptanpaşa landslide events designed based on the conditions without precipitation

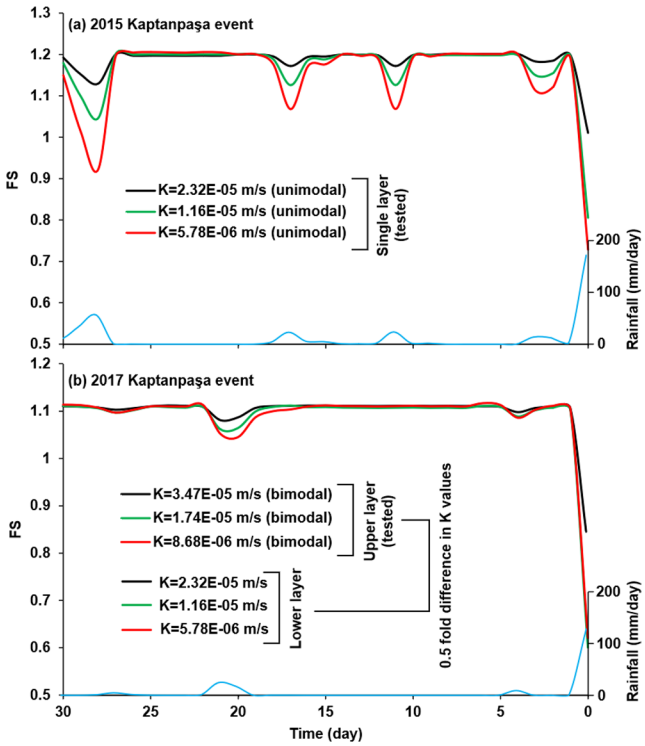

Fig. 12 Comparison of FS from **a**) the single-layer model (unimodal) and **b**) the two-layer model (bimodal) for different saturated permeabilities

fundamentally pre-conditions the soil for failure (Bogaard and Greco 2016; Luo et al. 2025; Smethurst et al. 2012). While previous studies have extensively documented the laboratory behavior of desiccation cracks under controlled drying-wetting cycles, this study contributes complementary site-scale numerical evidence and regional-scale statistical evidence that together are consistent with this localized physical mechanism contributing to landslide occurrence coupled with extreme meteorological forcing.

Due to the absence of direct measurements from the study area, saturated hydraulic conductivity values were adopted from the literature based on the soil classification by Uyeturk et al. (2020). Specifically, the k values taken as 2 m/day (2.32×10^{-5} m/s) for the single-layer model, while for the bimodal case, values of 3 m/day (3.47×10^{-5} m/s) and 2 m/day were used for the upper and lower layers, respectively. To further evaluate the parameter choices, different saturated hydraulic conductivity (k; Eq. 1) values were tested for both the single-layer model (Fig. 12a) and the two-layer model (Fig. 12b). For the single-layer (unimodal SWCC) case, k values were explored around the conceptual-model setting. For the two-layer (bimodal SWCC) case, k was varied only in the upper layer to represent enhanced permeability due to desiccation cracks, which are expected to affect the near-surface zone.

For all sensitivity analyses, the computational models were specifically executed for the final 30-day period preceding the landslide events to enhance the resolution of the graphs, allowing for a more detailed examination of the subtle FS fluctuations and the critical slope stability responses immediately preceding the landslide events on last day of the analysis.

Figure 12a shows that all three single-layer configurations exhibit similar overall FS behavior; stability decreases during rainfall and recovers during dry periods, but the fluctuation amplitude depends on k. The k value of 0.5 m/d (5.78×10^{-6} m/s; red line) produces the largest and most frequent FS drops, including multiple episodes with FS < 1.0. In contrast, the k value of 2 m/day (2.32×10^{-5} m/s; black line) best reproduces the 2015 Kaptanpaşa observations, where only a few landslides occurred on the day of intense rainfall. This supports our conceptual-model choice.

In the two-layer case (Fig. 12b), FS remains relatively stable across all three k tests, fluctuating narrowly around ~ 1.1, with a pronounced decline at the end of the simulation.

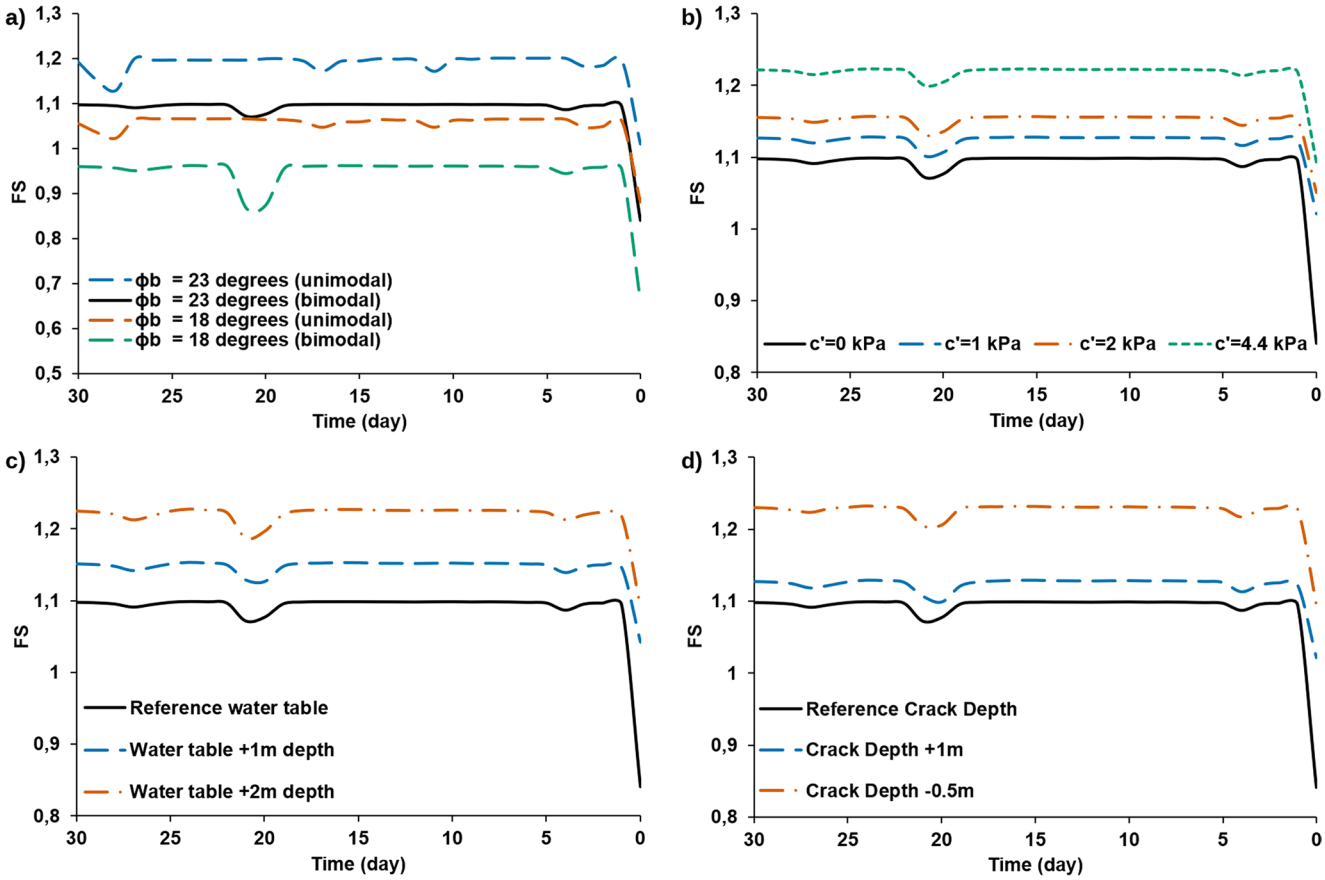

Fig. 13 Sensitivity of the factor of safety to key uncertain parameters in the two-layer (bimodal SWCC) model for the 2017 Kaptanpaşa dry-conditions scenario. (**a**) angle of shear strength increases with matric suction (ϕ^b), (**b**) effective cohesion of the cracked surface layer, (**c**) initial groundwater table depth and (**d**) depth of the cracked surface layer

Even the lowest-permeability test (red line) shows only slightly lower FS during minor infiltration, which indicates that the bimodal SWCC reduces FS sensitivity to k. This behavior is consistent with dual-porosity dynamics: macropores drain rapidly while micropores retain moisture, limiting pore-pressure buildup. All simulations display a sharp FS drop on last day in response to the major rainfall event. Although k still modulates the depth of this drop, the effect is subtler than in the unimodal system. Overall, the black-line k settings are taken as representative of the conceptual models. Similar results have been seen in the relevant literature for multilayer systems (Abbasov et al. 2024).

Another variable that we carried out a similar sensitivity analysis as above is ϕ^b. As mentioned in methodology section, the general assumption for ϕ^b is to be two-thirds of the effective internal friction angle (ϕ') (Aversa et al. 2016; Erdağ and Işık 2022). Here, this choice was tested with different values of φ^b between 18°, which corresponds to two-thirds of the φ' (27°) used in the numerical model, and 23° (Fig. 13a). Although the general trend remains consistent across both models, a higher ϕ^b results in increased unsaturated shear strength, thereby more impactful on FS. In the case of the bimodal SWCC model with ϕ^b= 18°, FS values remain below the critical threshold from the outset. Conversely, assigning ϕ^b a value of 23° yields FS estimates more consistent with the timing and occurrence of observed landslide events. Therefore, ϕ^b= 23° appears to be a more appropriate representation for the model.

In addition to the hydraulic conductivity and ϕb sensitivity analyses presented above, the sensitivity of the computed FS to the assumed c' of the cracked surface layer was evaluated, since this parameter cannot be independently measured for the study area. Holding the bimodal SWCC and all other parameters fixed at their reference values (Table 2), the 2017 dry-conditions model was re-run for c' = 0, 1, 2, and 4.4 kPa, spanning the full range from complete loss of cohesion to the intact value reported by Uyeturk et al. (2020) (Fig. 13b).

FS increased monotonically and smoothly with c' throughout the 60-day simulation period with all four curves converging to a common, sharp reduction at the time of the triggering rainfall event. At that point, FS reached ~0.84, ~1.02, ~1.05, and ~1.09 for c' = 0, 1, 2, and 4.4 kPa, respectively. Two observations follow from

this analysis. First, the qualitative outcome. FS approaching or falling below the critical threshold specifically at the triggering event, holds across the entire range of plausible cohesion degradation (0–2 kPa) considered here, and is not an artifact of the specific choice of c' = 0 kPa, even a partial loss of cohesion is sufficient to bring the slope close to its stability limit under the same hydro-meteorological forcing. Second, the transition from a clearly stable configuration (c' = 4.4 kPa, FS ≈ 1.10) to a marginally stable or failed one (c' ≤ 1 kPa, FS ≈ 1.0–1.02) occurs within a narrow, low range of cohesion values, underscoring that the computed factor of safety is highly sensitive to a parameter that is presently constrained only by qualitative literature evidence for crack-induced strength degradation (Pineda et al. 2014; Qi and Vanapalli 2015) rather than by direct measurement at this site.

Because the initial groundwater table used in the conceptual model was inferred from well observations located approximately 15 km from the study area rather than measured directly at the site, the sensitivity of the computed FS to this assumption was further tested by uniformly lowering the reference water table by 1 m and 2 m while holding all other parameters at their reference values (Fig. 13c). FS increased monotonically with water table depth throughout the 60-day simulation, from a baseline of ~1.10 (reference table) to ~1.15 (+1 m) and ~1.22 (+2 m), consistent with the expected reduction in pore-water pressure and corresponding increase in matric suction as the phreatic surface is lowered. At the time of the triggering rainfall event, FS reached ~0.84, ~1.04, and ~1.10 for the reference, +1 m, and +2 m water tables, respectively.

This result indicates that the predicted failure (FS < 1) is specific to the shallow, reference water table configuration, lowering the table by as little as 1 m is sufficient to keep the slope nominally stable throughout the entire simulation period, including during the triggering rainfall. Because the reference table depth is not directly constrained by site-specific measurements, this sensitivity underscores that the reported numerical result depends critically on an assumption that currently rests on regional rather than local hydrogeological evidence.

To evaluate the sensitivity of the computed FS to the assumed thickness of the cracked surface layer, the 2017 dry-conditions model was additionally re-run with the crack depth set to 2 m (+1 m relative to the reference) and 0.5 m (−0.5 m relative to the reference), holding the bimodal SWCC and all other parameters fixed at their reference values (Fig. 13d). FS remained relatively stable through most of the time window, reaching approximately 1.10, 1.13, and 1.23 by day 30 for the reference (1 m), +1 m, and −0.5 m configurations, respectively, before dropping sharply at the triggering rainfall event to approximately 0.84, 1.02, and 1.10. The response to crack depth was non-monotonic: both the thicker (2 m) and thinner (0.5 m) configurations yielded a higher FS than the 1 m reference depth. Inspection of the critical slip surfaces indicates that this pattern reflects a shift in failure geometry rather than the volume of weakened material alone: for the +1 m and −0.5 m configurations, the critical surface identified by the limit-equilibrium search is deeper than for the reference case, engaging a larger proportion of higher-cohesion intact soil and thereby yielding greater resisting strength along the slip surface. In the 1 m reference configuration, by contrast, the critical surface remains largely confined to the low-cohesion cracked layer, producing the lowest computed stability of the three.

Taken together, these sensitivity analyses indicate that the qualitative conclusion of this study is comparably sensitive to the assumed cohesion degradation, groundwater table depth, and cracked-layer thickness, each capable of shifting the computed FS at the triggering event by a similar magnitude ($\Delta \approx 0.25$), all of which currently rely on regional or literature-based rather than site-specific data. The model is also sensitive to the assumed ϕ^b though in a qualitatively different way: while both tested values (18° and 23°) produce a sharp FS decline at the triggering rainfall event, the lower bound ($\phi^b = 18°$) yields a bimodal-model FS trajectory that remains below the critical threshold for most of the antecedent period, inconsistent with the observed timing of the 2017 landslide; the upper bound ($\phi^b = 23°$) was therefore adopted as the more consistent representation (Sect. 4.1). The results are comparatively robust only to the assumed hydraulic conductivity within the tested range. The complete set of adopted parameters, their sources, and sensitivity status are summarized in Table S4.

While this study provides quantitative insights into the role of antecedent dry spells, several limitations should be acknowledged. First, and most fundamentally, no pre-failure or post-failure geotechnical survey data, slip-surface geometry, crack mapping, or site-specific soil profiles exist in the published literature or in the records of the relevant governmental disaster-management agencies for the landslide events examined here, precluding a site-calibrated back-analysis of any individual failure. The numerical framework was therefore designed, using a conceptual, regionally representative slope geometry, to evaluate the physical plausibility of the hypothesized drought–cracking–infiltration mechanism rather than to reproduce the specific failure conditions of an individual, field-documented landslide; the resulting factor-of-safety trends should therefore be interpreted as consistent with this hypothesis rather than as independent proof of it.

Second, no direct field evidence for desiccation cracking was available for this study: no pre-failure photographs, crack width/depth surveys, or infiltration tests were

conducted to confirm the presence, geometry, or hydraulic effect of surface cracks during the 2017 dry period. The bimodal SWCC, enhanced upper-layer hydraulic conductivity, and reduced surface cohesion adopted for the 2017 scenario therefore represent a conceptual, literature-informed hypothesis rather than a field-calibrated representation of the actual soil state, built on independent, indirect evidence, the sustained ~ 22 °C temperatures and near-absence of rainfall during the antecedent period, comparable to laboratory conditions under which desiccation cracks have been experimentally observed to initiate within days (Tang et al. 2010) and progressively deepen over drying-wetting cycles (Luo et al. 2025), combined with published relationships between crack formation and strength/permeability degradation in similar fine-grained soils (Pineda et al. 2014; Qi and Vanapalli 2015).

Third, the specific parameter values adopted to represent the cracked layer including saturated hydraulic conductivity, crack depth, and the degree of cohesion loss are based on literature values rather than site-specific measurements. The sensitivity analyses (Fig. 13b–d) indicate that the model's conclusions are particularly sensitive to the assumed cohesion loss and, to a lesser extent, crack depth and groundwater table position, whereas the results are comparatively robust to hydraulic conductivity within the tested range.

Fourth, the current model simplifies ecohydrological interactions; processes such as root water uptake and canopy interception were not considered. Plant root systems significantly alter soil permeability by creating natural preferential flow paths (macropores) while simultaneously providing mechanical root reinforcement. During prolonged droughts, the decay or shrinkage of roots may leave additional voids, further exacerbating rapid infiltration when intense rainfall occurs. Future studies should aim to incorporate these dynamic root-soil-water interactions into the coupled hydro-mechanical models.

Looking forward, extending this localized conceptual model to a regional scale presents a highly promising research direction. Utilizing Interferometric Synthetic Aperture Radar (InSAR) time-series analysis could allow for the large-scale monitoring of pre-failure deformations and the seasonal shrinking-swelling dynamics of clay-rich slopes. Observing these millimeter-scale surface displacements during dry-wet cycles would provide invaluable remote-sensing validation for the dual-porosity infiltration mechanics proposed in this study. Ultimately, coupling InSAR-derived deformation metrics with real-time field monitoring (e.g., tensiometers) and drought indices (such as SPI) could pave the way for a new generation of dynamic, spatially distributed landslide early warning systems.

Conclusions

This study provides compelling evidence that antecedent dry spells can significantly modulate the occurrence and magnitude of rainfall-induced shallow landslides, in clay size environments such as those found in the eastern Black Sea region of Türkiye.

By integrating physically based numerical simulations with data-driven statistical modeling, it was demonstrated that the timing and hydro-meteorological context of rainfall events play a critical role in slope instability.

The numerical results reveal that desiccation-driven changes in soil hydraulic properties, particularly increased permeability and reduced shear strength, can accelerate infiltration and reduce slope stability during subsequent rainfall events. The use of bimodal soil-water characteristic curves effectively captures the influence of surface cracking and offers a more realistic representation of infiltration dynamics in desiccated soils.

Complementing the physical model, the data-driven analysis using a GAM further underscores the importance of antecedent conditions. Specifically, the interaction between low values of the SPI and high rainfall intensity emerged as a strong predictor of landslide occurrence.

These findings imply a critical limitation of conventional rainfall-threshold-based landslide predictive models that often neglect the antecedent dryness of the soil. Taken together, these findings emphasize that dry spells preceding intense rainfall events are not merely passive background conditions but active contributors to landslide hazard. Future landslide early warning systems would benefit from incorporating drought metrics alongside traditional rainfall thresholds. Given the increasing frequency of extreme weather patterns driven by climate change, such an integrated approach is not only timely but essential for improving the predictive capacity and resilience of landslide-prone regions.

Supplementary Information The online version contains supplementary material available at https://doi.org/10.1007/s12665-026-13171-1.

Acknowledgements This study was conducted as part of Dogukan Tayyar's doctoral dissertation at Hacettepe University. The corresponding author is grateful to the International Research Fellowship Programme for PhD Students (BİDEB 2214-A) of the Scientific and Technological Research Council of Turkey (TÜBİTAK) (Application Number: 1059B142401302) and Hacettepe University Scientific Research Projects Coordination Unit (Project No: FHD-2024-21082) for supporting this study. The authors also express their gratitude to Geological Engineers Eroltan Durmuş and Yaşar Özdoğan for their support.

Author contributions D.T. : Conceptualization, Methodology, Software, Validation, Formal analysis, Investigation, Writing - Original Draft, Writing - Review & Editing, VisualizationH.T. : Conceptu-

alization, Methodology, Software, Validation, Formal analysis, Investigation, Writing - Original Draft, Writing - Review & Editing, VisualizationR.C. : Methodology, Formal analysis, Data CurationA.Y. : Writing - Original Draft, Writing - Review & EditingT.G. : Conceptualization, InvestigationN.S.I. : Conceptualization, Methodology, Software, Validation, Writing - Review & EditingM.E. : Conceptualization, Methodology, Software, Validation, Writing - Review & Editing.

Data availability The data are available upon request.

Declaration

Competing interests The authors declare no competing interests.

Open Access This article is licensed under a Creative Commons Attribution 4.0 International License, which permits use, sharing, adaptation, distribution and reproduction in any medium or format, as long as you give appropriate credit to the original author(s) and the source, provide a link to the Creative Commons licence, and indicate if changes were made. The images or other third party material in this article are included in the article's Creative Commons licence, unless indicated otherwise in a credit line to the material. If material is not included in the article's Creative Commons licence and your intended use is not permitted by statutory regulation or exceeds the permitted use, you will need to obtain permission directly from the copyright holder. To view a copy of this licence, visit http://creativecommons.org/licenses/by/4.0/.

References

Abbasov R, Fahs M, Younes A, Nowamooz H, Måløy KJ, Toussaint R (2024) Modeling rainfall-induced landslide using the concept of local factor of safety: uncertainty propagation and sensitivity analysis. Comput Geotech 167:106102

Ahmed M, Tanyas H, Huser R et al (2023) Dynamic rainfall-induced landslide susceptibility: a step towards a unified forecasting system. Int J Appl Earth Obs Geoinf 125:103593. https://doi.org/10.1016/j.jag.2023.103593

Alan I, Balcı V, Keskin H, Altun I, Böke N, Demirbag H, Arman S, Elibol H, Soyakil M, Kop A, Hanilçi N (2019) Bulletin of the Mineral Research and Exploration notes to the authors. Bull Min Res Explor 158:1–29. https://doi.org/10.19076/mta.19369

Alvioli M, Marchesini I, Reichenbach P, Rossi M, Ardizzone F, Fiorucci F, Guzzetti F (2016) Automatic delineation of geomorphological slope units with r.slopeunits v1.0 and their optimization for landslide susceptibility modeling, Geosci Model Dev 9:3975–3991. https://doi.org/10.5194/gmd-9-3975-2016

Apriyono A, Yuliana Y, Kamchoom V, Leung AK, Jotisankasa A, Liangtong Z (2025) The effect of desiccation cracks on water infiltration in landfill cover under extreme climate scenarios. Waste Manag 196:10–21

Aversa S, Cascini L, Picarelli L, Scavia C (eds) (2016) Landslides and engineered slopes: experience, theory and practice, 1st edn. CRC, Italy

Banfi F, Bevacqua E, Rivoire P, Oliveira SC, Pinto JG, Ramos AM, De Michele C (2023) Temporal clustering of precipitation for detection of potential landslides. Nat Hazards Earth Syst Sci Discuss 2023:1–21

Baum RL, Godt JW (2010) Early warning of rainfall-induced shallow landslides and debris flows in the USA. Landslides 7:259–272. https://doi.org/10.1007/s10346-009-0177-0

Bhadiyadra K, Ong DE (2024) Mechanics of rainfall-induced landslides after a prolonged dry period based on laboratory tests and numerical models incorporating soil-water characteristic curves. Geosciences 14:174

Biniak-Pieróg M, Chalfen M, Żyromski A, Doroszewski A, Jóźwicki T (2020) The soil moisture during dry spells model and its verification. Resources 9:85

Bogaard TA, Greco R (2016) Landslide hydrology: from hydrology to pore pressure. WIREs Water 3:439–459

Brenning A (2008) Statistical geocomputing combining R and SAGA: the example of landslide susceptibility analysis with generalized additive models. Hambg Beitr Phys Geogr Landschaftsökologie 19:410

Brier GW (1950) Verification of forecasts expressed in terms of probability. Mon Weather Rev 78(1):1–3

Cheng Q, Tang CS, Xu D, Zeng H, Shi B (2021) Water infiltration in a cracked soil considering effect of drying-wetting cycles. J Hydrol 593:125640. https://doi.org/10.1016/j.jhydrol.2020.125640

Çömert R, Tanyaş H, Lombardo L, Görüm T (2025) An open event-inventory database of rainfall-induced landslides and their environmental characteristics in the eastern Black Sea region of Türkiye. Eng Geol 108258 https://doi.org/10.1016/j.enggeo.2025.108258.

Crosta G (1998) Regionalization of rainfall thresholds: an aid to landslide hazard evaluation. Environ Geol 35:131–145

Dakshanamurthy V, Raman V (1973) A simple method of identifying an expansive soil. Soils Found 13:97–104

Damiano E, Greco R, Guida A, Olivares L, Picarelli L (2017) Investigation on rainwater infiltration into layered shallow covers in pyroclastic soils and its effect on slope stability. Eng Geol 220:208–218. https://doi.org/10.1016/j.enggeo.2017.02.006

Dos Santos JCN, de Andrade EM, Guerreiro MJS, Medeiros PHA, de Queiroz Palácio HA, de Araújo Neto JR (2016) Effect of dry spells and soil cracking on runoff generation in a semiarid micro watershed under land use change. J Hydrol 541:1057–1066

Durmaz M (2022) Physically-based modeling of rainfall-triggered landslides in Kaptanpaşa, Rize. Dissertation, Middle East Technical University

Durmaz M, Hürlimann M, Huvaj N, Medina V (2023) Comparison of different hydrological and stability assumptions for physically-based modeling of shallow landslides. Eng Geol 323:107237

Edwards DC, McKee TB (1997) Characteristics of 20th century drought in the United States at multiple time scales. Colorado State University, Fort Collins

Erdağ A, Işık NS (2022) Effect of rainfall intensity on the stability of unsaturated slopes of silty clay soils of Kazan, Ankara, Turkey. Arab J Geosci 15:894

Fang Z, Tanyas H, Gorum T et al (2023) Speech-recognition in landslide predictive modelling: a case for a next generation early warning system. Environ Model Softw 170:105833. https://doi.org/10.1016/j.envsoft.2023.105833

Fawcett T (2006) An introduction to ROC analysis. Pattern Recognit Lett 27:861–874. https://doi.org/10.1016/j.patrec.2005.10.010

Fredlund DG, Morgenstern NR, Widger RA (1978) The shear strength of unsaturated soils. Can Geotech J 15:313–321

Fredlund DG, Houston SL, Nguyen Q, Fredlund MD (2010) Moisture movement through cracked clay soil profiles. Geotech Geol Eng 28:865–888

Funk C, Peterson P, Landsfeld M et al (2015) The climate hazards infrared precipitation with stations - a new environmental record for monitoring extremes. Sci Data 2:150066. https://doi.org/10.1038/sdata.2015.66

Gao H, An R, Zhang X, Wang G, Liu X, Xu Y (2024) Dynamic evolution of desiccation cracks and their relationship with the hydraulic properties of expansive soil. Int J Geomech 24:04023299

Gasmo JM, Rahardjo H, Leong EC (2000) Infiltration effects on stability of a residual soil slope. Comput Geotech 26:145–165

Gedik A, Ercan T, Korkmaz S, Karatas S (1992) Rize-Fındıklı-Çamlıhemşin arasında (Doğu Karadeniz) yer alan magmatik kayaçların petrolojisi ve Doğu Pontidlerdeki bölgesel yayılımları. Türkiye Jeol Kurumu Bül 35:15–38 (in Turkish)

Görüm T, Fidan S (2021) Spatiotemporal variations of fatal landslides in Turkey. Landslides. https://doi.org/10.1007/s10346-020-01580-7

Greco R, Marino P, Bogaard TA (2023) Recent advancements of landslide hydrology. WIREs Water 10:e1675

Guzzetti F, Gariano SL, Peruccacci S et al (2020) Geographical landslide early warning systems. Earth Sci Rev 200:102973. https://doi.org/10.1016/j.earscirev.2019.102973

Haque U, Blum P, Da Silva PF et al (2016) Fatal landslides in Europe. Landslides 13:1545–1554

Hassanikhah A, Miller GA, Cerato AB (2022) A method to predict desiccation crack depth in a compacted clayey soil. Can Geotech J 59:526–537

Holtz WG, Gibbs HJ (1956) Engineering properties of expansive clays. Trans Am Soc Civ Eng 121:641–663

Jayakody SHS, Uzuoka R, Ueda K, Xu J (2023) Unsaturated slopes behavior under antecedent intermittent rainfall patterns: centrifuge and numerical study. Acta Geotech 18:5773–5790

Joussein E, Petit S, Churchman J, Theng B, Righi D, Delvaux BJCM (2005) Halloysite clay minerals - a review. Clay Min 40:383–426

Keles F, Nefeslioglu HA (2021) Infinite slope stability model and steady-state hydrology-based shallow landslide susceptibility evaluations: the Guneysu catchment area (Rize, Turkey). CATENA 200:105161

Li JH, Zhang LM, Li X (2011) Soil-water characteristic curve and hydraulic conductivity function for unsaturated cracked soil. Can Geotech J 48:1010–1031. https://doi.org/10.1139/t11-027

Li WC, Dai FC, Wei YQ, Wang ML, Min H, Lee LM (2016) Implication of subsurface flow on rainfall-induced landslide: a case study. Landslides 13:1109–1123

Lim J, Santinelli G, Dahal A, Vrieling A, Lombardo L (2024) An ensemble neural network approach for space-time landslide predictive modelling. Int J Appl Earth Obs Geoinf 132:104037

Luo Y, Zhang J, Zhou Z, Aguilar-Lopez JP, Greco R, Bogaard T (2023) Effects of dynamic changes of desiccation cracks on preferential flow: experimental investigation and numerical modeling. Hydrol Earth Syst Sci 27:783–808

Luo Y, Zhang J, Tang CS, Jiang G, Bogaard T (2025) Impact of dynamic desiccation cracks on hydrological processes and stability in expansive clay slopes: a coupled dual-permeability modeling approach. Eng Geol 108377

Marino P, Peres DJ, Cancelliere A et al (2020) Soil moisture information can improve shallow landslide forecasting using the hydrometeorological threshold approach. Landslides 17:2041–2054

McKee TB, Doesken NJ, Kleist J (1993) The relationship of drought frequency and duration to time scales. In: Proceedings of the 8th Conference on Applied Climatology, California, pp 179–183

Mondini AC, Guzzetti F, Melillo M (2023) Deep learning forecast of rainfall-induced shallow landslides. Nat Commun 14:2466. https://doi.org/10.1038/s41467-023-38135-y

Moreno M, Lombardo L, Steger S, de Vugt L, Zieher T, Crespi A et al (2025) Functional regression for space-time prediction of precipitation-induced shallow landslides in South Tyrol, Italy. J Geophys Res Earth Surf 130:e2024JF008219

National Drought Mitigation Center (2018) SPI Generator [software]. University of Nebraska-Lincoln. https://drought.unl.edu/Monitoring/SPI/SPIProgram.aspx

Nefeslioglu HA, Gokceoglu C, Sonmez H, Gorum T (2011) Medium-scale hazard mapping for shallow landslide initiation: the Buyukkoy catchment area (Cayeli, Rize, Turkey). Landslides 8:459–483. https://doi.org/10.1007/s10346-011-0267-7

Nocentini N, Rosi A, Segoni S, Fanti R (2023) Towards landslide space-time forecasting through machine learning: the influence of rainfall parameters and model setting. Front Earth Sci 11:1152130

Piciullo L, Calvello M, Cepeda JM (2018) Territorial early warning systems for rainfall-induced landslides. Earth Sci Rev 179:228–247. https://doi.org/10.1016/j.earscirev.2018.02.013

Pineda JA, Romero E, Gracia MD, Sheng D (2014) Shear strength degradation in claystones due to environmental effects. Géotechnique 64:493–501. https://doi.org/10.1680/geot.13.T.025

Planet Team (2017) Planet Application Program Interface: space for life on Earth. Planet Labs, San Francisco. https://api.planet.com

Pouya A, Vo TD, Hemmati S, Tang AM (2019) Modeling soil desiccation cracking by analytical and numerical approaches. Int J Numer Anal Methods Geomech 43:738–763

Qi S, Vanapalli SK (2015) Hydro-mechanical coupling effect on surficial layer stability of unsaturated expansive soil slopes. Comput Geotech 70:68–82

R Core Team (2026) R: A language and environment for statistical computing. R Foundation for Statistical Computing, Vienna, Austria

Rahardjo H, Ong TH, Rezaur RB, Leong EC (2007) Factors controlling instability of homogeneous soil slopes under rainfall. J Geotech Geoenviron Eng 133:1532–1543

Reis S, Nişanci R, Yomralioğlu T (2009) Designing and developing a province-based spatial database for the analysis of potential environmental issues in Trabzon, Turkey. Environ Eng Sci 26:123–130. https://doi.org/10.1089/ees.2007.0158

Saito T, Rehmsmeier M (2015) The precision-recall plot is more informative than the ROC plot when evaluating binary classifiers on imbalanced datasets. PLoS ONE 10(3):e0118432

Sander T, Gerke HH (2007) Preferential flow patterns in paddy fields using a dye tracer. Vadose Zone J 6:105–115. https://doi.org/10.2136/vzj2006.0035

Schulz WH, Smith JB, Wang G et al (2018) Clayey landslide initiation and acceleration strongly modulated by soil swelling. Geophys Res Lett 45:1888–1896. https://doi.org/10.1002/2017GL076807

Seequent Limited (2022) Heat and mass transfer modeling (GeoStudio documentation). Seequent, Christchurch

Segoni S, Battistini A, Rossi G, Rosi A, Lagomarsino D, Catani F, Moretti S, Casagli N (2015) An operational landslide early warning system at regional scale based on space-time-variable rainfall thresholds. Nat Hazards Earth Syst Sci 15:853–861

Segoni S, Piciullo L, Gariano SL (2018) A review of the recent literature on rainfall thresholds for landslide occurrence. Landslides 15:1483–1501. https://doi.org/10.1007/s10346-018-0966-4

Skempton AW (1953) The colloidal activity of clays. In: Proceedings of the 3rd international conference on soil mechanics and foundation engineering, Zurich, vol 1. pp 57–61

Smethurst JA, Clarke D, Powrie W (2012) Factors controlling the seasonal variation in soil water content and pore water pressures within a lightly vegetated clay slope. Géotechnique 62:429–446

Stanley TA, Kirschbaum DB, Benz G et al (2021) Data-driven landslide nowcasting at the global scale. Front Earth Sci 9

Stirling RA, Toll DG, Glendinning S, Helm PR, Yildiz A, Hughes PN, Asquith JD (2021) Weather-driven deterioration processes affecting the performance of embankment slopes. Géotechnique 71:957–969. https://doi.org/10.1680/jgeot.19.SiP.038

Tang CS, Cui YJ, Tang AM, Shi B (2010) Experimental evidence on the temperature dependence of desiccation cracking behavior of clayey soils. Eng Geol 114:261–266

Tanyaş H, Görüm T, Kirschbaum D, Lombardo L (2022) Could road constructions be more hazardous than an earthquake in terms of mass movement? Nat Hazards. https://doi.org/10.1007/s11069-021-05199-2

Terzaghi K (1950) Mechanism of landslides. In: Paige S (ed) Application of geology to engineering practice (Berkey volume). Geological Society of America, New York, pp 83–123

Thornthwaite CW (1948) An approach toward a rational classification of climate. Geogr Rev 38:55–94

Tichavský R, Ballesteros-Cánovas JA, Šilhán K et al (2019) Dry spells and extreme precipitation are the main trigger of landslides in Central Europe. Sci Rep 9:14560. https://doi.org/10.1038/s41598-019-51148-2

Tsaparas I, Rahardjo H, Toll DG, Leong EC (2002) Controlling parameters for rainfall-induced landslides. Comput Geotech 29:1–27

Tuysuz O, Genc S, Tarı U, Erturac M (2008) Geological, geographical and manmade factors controlling landslide potential of Rize province, Northern Turkey. In: 33rd International Geological Congress, Oslo

Uyeturk CE (2019) Geotechnical characterization of soils prone to rainfall-induced landslides in Rize (northern Turkey). Dissertation, Middle East Technical University

Uyeturk CE, Huvaj N, Bayraktaroglu H, Huseyinpasaoglu M (2020) Geotechnical characteristics of residual soils in rainfall-triggered landslides in Rize, Turkey. Eng Geol 264:105318

Vanapalli SK, Fredlund DG, Pufahl DE, Clifton AW (1996) Model for the prediction of shear strength with respect to soil suction. Can Geotech J 33:379–392

Wicki A, Lehmann P, Hauck C et al (2020) Assessing the potential of soil moisture measurements for regional landslide early warning. Landslides 17:1881–1896. https://doi.org/10.1007/s10346-020-01400-y

Wood SN (2017) Generalized Additive Models: An Introduction with R, 2nd edn. Chapman and Hall/CRC, Boca Raton

Wood SN, Scheipl F, Faraway JJ (2013) Straightforward intermediate rank tensor product smoothing in mixed models. Stat Comput 23(3):341–360

Yalcin A (2007) Environmental impacts of landslides: a case study from East Black Sea region, Turkey. Environ Eng Sci 24:821–833. https://doi.org/10.1089/ees.2006.0161

Yüksek Ö, Kankal M, Üçüncü O (2013) Assessment of big floods in the Eastern Black Sea Basin of Turkey. Environ Monit Assess 185:797–814. https://doi.org/10.1007/s10661-012-2592-2

Zhang CL, Li TL, Li P (2014) Rainfall infiltration in Chinese loess by in situ observation. J Hydrol Eng 19:159. https://doi.org/10.1061/(ASCE)HE.1943-5584.0001015

Zhang JM, Luo Y, Zhou Z, Chong L, Victor C, Zhang YF (2021) Effects of preferential flow induced by desiccation cracks on slope stability. Eng Geol 288:106164

Zhao B, Dai Q, Han D et al (2019) Probabilistic thresholds for landslides warning by integrating soil moisture conditions with rainfall thresholds. J Hydrol 574:276–287. https://doi.org/10.1016/j.jhydrol.2019.04.062

Zhuo L, Dai Q, Han D et al (2019) Evaluation of remotely sensed soil moisture for landslide hazard assessment. IEEE J Sel Top Appl Earth Obs Remote Sens 12:162–173. https://doi.org/10.1109/JSTARS.2018.2883361

Publisher's note Springer Nature remains neutral with regard to jurisdictional claims in published maps and institutional affiliations.